

The ordinary Kohn method also suffers from the problem of sporadic singularities⁸ in the estimated amplitude, which is related to the fact that one must work at a value of E in the spectrum of the operator $T+V$. In the new method, E is not in the spectrum of $\theta^2 T+V_\theta$, and we expect that no convergence problems will arise. We believe that, for the numerical example discussed above, it is possible to prove the convergence of the method, but the details will not be presented here.

The scheme proposed here may also be superior to the method of analytic continuation from negative E suggested by Schlessinger and Schwartz⁹ and recently

⁸ C. Schwartz, *Ann. Phys. (N. Y.)* **16**, 36 (1961).

⁹ L. Schlessinger and C. Schwartz, *Phys. Rev. Letters* **16**, 1173 (1966).

generalized¹⁰ to include complex E . The effort required to do the computations should be similar in these two approaches, but no continuation with its attendant errors is now needed. In some circumstances it might be advantageous to combine the two methods.

Note added in proof. Dr. Charles Schwartz has kindly pointed out that a coordinate rotation has been previously used in the two-particle problem by T. Regge [*Nuovo Cimento* **14**, 951 (1959)] and R. Haymaker [University of California Report No. UCRL-17652, Part VIII, 1967 (unpublished)].

ACKNOWLEDGMENT

We are grateful to Dr. G. D. McCartor for helpful discussions.

¹⁰ F. A. McDonald and J. Nuttall, *Phys. Rev. Letters* **23**, 361 (1969).

Proton-Neutron Final-State Interaction

D. P. BOYD†*

Rutgers, The State University, New Brunswick, New Jersey 08903

AND

P. F. DONOVAN‡ AND J. F. MOLLENAUER

Bell Telephone Laboratories, Murray Hill, New Jersey 07974

(Received 9 July 1969)

The reactions $p(d, 2p)n$ and $d(p, 2p)n$ were studied at a proton bombarding energy of 16.0 MeV and deuteron bombarding energies of 16.0 and 10.0 MeV. The protons were detected in coincidence with solid-state detectors at angles that allow strong enhancement of the p - n final-state interaction. The coincidence resolving time was sharpened by using time-energy correlation techniques that utilize an on-line SDS-910 computer. The data were analyzed using the "data-simulation technique." A simple theory, which, apart from normalization, contained three adjustable parameters, was found to produce satisfactory fits. In this theory, the final-state interactions are accounted for by assuming additive enhancements for each pair of final-state particles and each spin state. The primary interaction is approximated by the sum of a constant amplitude plus the spectator-effect amplitude. The widths of the final-state interaction peaks are in good agreement with Watson theory using the known singlet p - n scattering length a_{np}^s of -23.69 F. The most accurately determined scattering length was extracted from the 16-MeV $p+d$ data and was $a_{np}^s = -23.8 \pm 0.5$ F. This agreement indicates that interference effects are not important in this reaction at center-of-mass energies above a few MeV if coincidence techniques are employed. With similar methods, a comparative study of the $n+d$ reaction in order to measure the singlet n - n scattering length should be fruitful.

I. INTRODUCTION

A. Three-Body Experiments and Nucleon-Nucleon Interaction

THE nucleon-nucleon interaction plays a fundamental role in our understanding of nuclear physics. Unfortunately, our knowledge of this interaction is incomplete, and there are presently several theoretical potentials that describe the existing two-body scattering

data equally well.¹ The study of three-body reactions can, in principle, contribute new information to our knowledge of the nucleon-nucleon interaction in two ways. The first is through investigation of the off-the-energy-shell behavior of the nucleon-nucleon potential, which is, for example, currently being studied in n - p and p - p bremsstrahlung experiments. Quasifree scattering experiments also provide knowledge of the off-the-energy-shell behavior.

The second class of three-body experiments that give nucleon-nucleon potential information consists of those that investigate the neutron-neutron scattering in a final-state interaction, using a reaction such as $n+d \rightarrow$

† Present address: Bell Telephone Laboratories, Murray Hill, N. J.

* This work is taken from the Ph.D. thesis submitted to Rutgers University, 1968, and was supported in part by the National Science Foundation.

‡ Present address: National Science Foundation, Washington, D. C.

¹ See *Rev. Mod. Phys.* **39**, (1967).

$p+n+n$. Since the p - p scattering length is well known from two-body experiments, charge symmetry can be invoked to predict the n - n scattering length. However, the way in which the electromagnetic corrections are applied depends sensitively on the form of the nuclear potential used. For example, if one assumes charge symmetry and tries to calculate the singlet n - n scattering length a_{nn}^s , by unfolding the effects of the point Coulomb interaction from the p - p scattering data, it is found that the calculated n - n scattering length can vary from -16.4 to -19.3 F, depending on whether a hard-core potential or velocity-dependent potential is used.² A measurement of a_{nn}^s to better than 5% would provide valuable information about the fine details of nucleon-nucleon interaction. It is clearly important to obtain information on a_{nn}^s using a variety of techniques, since the extraction of this parameter from experimental data on systems containing three strongly interacting particles in either the initial or the final state is necessarily subject to some theoretical uncertainty.

Various forms of final-state interaction theory, as introduced by Watson³ in 1952, have enjoyed success in nuclear physics. In addition, this theory is often used in high-energy physics to investigate the interactions between elementary particles. However, the interpretation of these experiments depends on the validity of the assumptions employed in the final-state interaction theory that is used. These assumptions can best be tested in low-energy nuclear physics, where measurements of high precision can be made, and where the scattering parameters are often known accurately from two-body elastic scattering data.

The Watson final-state interaction theory has been applied by many groups to extract nucleon-nucleon scattering lengths in reactions such as $d(n, p)2n$, $t(n, d)2n$, $\text{He}^3(p, d)2p$, $\text{He}^3(n, d)np$, $\text{He}^3(\text{He}^3, \text{He}^4)2p$, and others⁴⁻¹⁵ However, the results have often not been mutually consistent and are usually not in agreement with the known scattering lengths. This seems to be due

² I. Slaus, Rev. Mod. Phys. **39**, 576 (1967).

³ K. M. Watson, Phys. Rev. **88**, 1163 (1952).

⁴ K. Ilakovac, C. G. Kuo, M. Petracic, I. Slaus, and P. Tomas, Nucl. Phys. **43**, 254 (1963).

⁵ E. Bar-Avraham, R. Fox, Y. Porath, G. Adam, and G. Frieder, Nucl. Phys. **B1**, 49 (1967).

⁶ W. T. H. Van Oers and I. Slaus, Phys. Rev. **160**, 853 (1967).

⁷ A. D. Bacher, T. A. Tombrello, and Y. S. Chen, Bull. Am. Phys. Soc. **11**, 896 (1966).

⁸ K. Nagatani and T. A. Tombrello, Bull. Am. Phys. Soc. **12**, 1139 (1967).

⁹ A. D. Bacher and T. A. Tombrello, Bull. Am. Phys. Soc. **12**, 1138 (1967).

¹⁰ E. Gross, J. Malanify, B. Morton, and A. Zucker, Bull. Am. Phys. Soc. **12**, 465 (1967).

¹¹ R. J. Slobodrian, J. S. C. McKee, W. F. Tivol, D. J. Clark, and T. A. Tombrello, Phys. Letters **25B**, 19 (1967).

¹² T. A. Tombrello and A. D. Bacher, Phys. Letters **17**, 37 (1956).

¹³ E. Baumgartner, H. E. Conzett, E. Shield, and R. J. Slobodrian, Phys. Rev. Letters **16**, 105 (1966).

¹⁴ H. T. Larson, A. D. Bacher, and T. A. Tombrello, Bull. Am. Phys. Soc. **12**, 465 (1967).

¹⁵ H. T. Larson and K. Nagatani, Bull. Am. Phys. Soc. **12**, 1139 (1967).

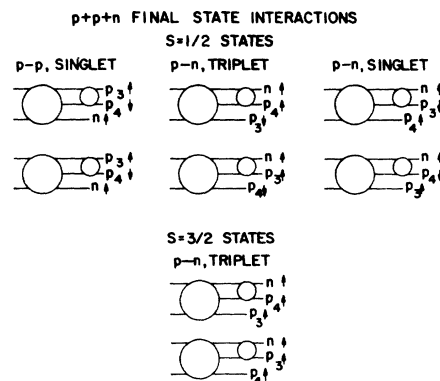


FIG. 1. Possible single final-state interaction diagrams. A deuteron and proton interact on the left in the large circle, which represents the primary interaction. The final-state interaction is represented by the small circle on the right, and various possible spin states are indicated.

to the inability, in experiments that measure the energy spectrum of only one final-state particle, to allow separation of the effects of the primary reaction mechanism from those of the final-state interaction, as explained in Sec. II A.

These difficulties can be largely removed through experiments that measure in coincidence the momentum of two of the three outgoing particles. The first attempt to extract a scattering length by analysis of such a coincident experiment was reported by Kim and Kane.¹⁶ They applied the theory of Frank and Gammel¹⁷ to the reaction $d(p, 2p)n$ and extracted a singlet p - n scattering length with an accuracy of ± 10 F. This reaction has recently been studied more extensively.¹⁸⁻²²

The experiments presented here are the result of a program designed to test with greatly improved precision the validity of final-state interaction theory as applied to the extraction of a_{pn}^s from the $d(p, 2p)n$ reaction. A range of center-of-mass energies from 1.1 to 8.44 MeV was investigated. The detector angles were chosen to allow enhancement of the proton-neutron final-state interaction. The data were analyzed using a simple model described in Sec. I D and IV E, which assumes that only two of the three final-state particles

¹⁶ Y. E. Kim and J. V. Kane, Rev. Mod. Phys. **37**, 519 (1965).

¹⁷ R. M. Frank and J. L. Gammel, Phys. Rev. **93**, 463 (1954).

¹⁸ W. Dwain Simpson, W. R. Jackson, and G. C. Phillips, Nucl. Phys. **A103**, 97 (1967).

¹⁹ A. Nüiler, C. Joseph, and G. C. Phillips, Bull. Am. Phys. Soc. **13**, 569 (1968); A. Nüiler, C. Joseph, V. Valkovic, W. von Witsch, and G. Phillips, Phys. Rev. **182**, 1083 (1969).

²⁰ D. Boyd, D. J. Bredin, J. P. F. Sellschop, J. F. Mollenauer, Č. Zupančič, and P. F. Donovan, Bull. Am. Phys. Soc. **12**, 34 (1967).

²¹ P. F. Donovan, J. F. Mollenauer, D. Boyd, and Č. Zupančič, in Proceedings of the International Conference on Nuclear Structure, Tokyo, 1967, p. 620 (unpublished); D. Boyd, P. F. Donovan, B. Marsh, and P. Assimakopoulos, Bull. Am. Phys. Soc. **13**, 567 (1968).

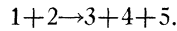
²² H. Brückmann, W. Gehrke, W. Kluge, H. Matthäy, L. Schänzler, and K. Wick, Report of Institute für Experimentelle Kernphysik der Universität und der Kernforschungszentrums, Karlsruhe, Germany (unpublished).

interact. This model takes into account contributions both from resonant and nonresonant processes, including "spectator" effects.

Experimental broadening effects were accounted for by using the "data-simulation" technique as explained in Sec. II B. The computer program that generates the simulated data is described in the Appendix (see also Ref. 23).

B. Kinematics of Three-Particle Reactions

We consider reactions of the following form:



The nine scalar momentum components of the final state completely specify the kinematics of the system. Four components can be eliminated by applying the conservation of energy and momentum. Thus the measurement of five independent scalar variables suffices.

In coincidence experiments, two of the particles (by our convention, particles 3 and 4) are detected at fixed angles. Thus six scalar variables are measured: the beam energy, two final-state particle energies, two angles with respect to the beam axis, and the azimuthal angle between the two detected particles. This constitutes a kinematic over specification of the system, which is useful in reducing background.

Conservation of energy and momentum restricts the energies of the two detected particles to values given by the following equation²⁴:

$$Q = (1+m_3/m_5)T_3 + (1+m_1/m_5)T_4 - (1-m_1/m_5)T_1 \\ - 2\cos\theta_3[(m_3m_1/m_5^2)T_1T_3]^{1/2} \\ - 2\cos\theta_4[(m_4m_1/m_5^2)T_1T_4]^{1/2} \\ + 2\cos\theta_{34}[(m_3m_4/m_5^2)T_3T_4]^{1/2}, \quad (1)$$

where

$$\cos\theta_{34} = \cos\theta_3\cos\theta_4 + \sin\theta_3\sin\theta_4\cos(\varphi_3 - \varphi_4).$$

The θ_i , φ_i , m_i , and T_i are the polar angles, azimuthal angles, masses, and energies of particle i ; Q is the Q value of the reaction. This is the equation of a fourth-degree curve in the T_3 - T_4 experimental space. Particle 5 is free to assume various momenta consistent with each T_3 , T_4 solution of Eq. (1). Each point on the T_3 , T_4 curve corresponds to a definite relative energy between each pair of particles. The occurrence of a resonance at a particular relative energy results in an enhancement or peak in the three-body cross section at the appropriate point on the T_3 - T_4 curve. An experiment at fixed angles and fixed incident energy may contain several peaks corresponding to resonances at various internal relative energies. It is convenient to formulate a theory

in terms of relative momenta, since they are Galilean invariants and may be calculated in any inertial system.

Calculations of three-body kinematics are in general too lengthy to perform by hand, and computer methods are necessary. The problem that is presented to the computer is to calculate the momentum of each of the three final-state particles, given the angles of the two detected particles and the energy of one of them. The computer also calculates the various relative energies in the intermediate two-particle systems. Because of the accuracy with which the experiment measures proton energies, a relativistic version of Eq. (1) is used.

The derivation of many useful three-particle kinematic formulas has been published by Ohlsen,²⁵ and the general case of n particles has been treated by Zupančič.²⁶ These two authors also give phase-space expressions, which are discussed in Sec. I E. The solution of the relativistic version of Eq. (1) was worked out by Kane²⁷ in the following form:

$$P_1 = \{-bc \pm [b^2(c^2 - 1) - 4a^2m_4^2]^{1/2}\} / (c^2 - 4a^2),$$

where

$$a = T_1 + m_1 + m_2 - T_3 - m_3,$$

$$b = P_1^2 + P_3^2 - 2P_3P_1\cos\theta_3 + m_3^2 - m_1^2 - a^2,$$

$$c = 2P_3[\cos\theta_3\cos\theta_1 + \sin\theta_3\sin\theta_1\cos(\phi_3 - \phi_1)] - 2P_1\cos\theta_4,$$

and the m_i , P_i , and T_i are the masses, momenta, and kinetic energies of particle i in units such that $c=1$. The angular coordinate system is defined so that the z axis is in the direction of the beam, and the y axis is perpendicular to the plane defined by the beam axis and the two coplanar detector centers.

The momentum of particle 5 is then given by

$$\mathbf{P}_5 = \mathbf{P}_1 - \mathbf{P}_3 - \mathbf{P}_4,$$

and the total and kinetic energies of particle i by

$$E_i^2 = P_i^2c^2 - m_i^2c^4,$$

$$T_i = E_i - m_i c^2.$$

The relative momenta of particles i and j are defined as

$$P_{ij \text{ rel}} = M_{ij} v_{ij \text{ rel}} = \frac{m_i m_j}{m_i + m_j} \left| \frac{\mathbf{P}_i}{m_i} - \frac{\mathbf{P}_j}{m_j} \right|,$$

and the relative wave number k is

$$k = P_{ij \text{ rel}} / \hbar.$$

C. Theory of Final-State Interactions

In many types of three-body reactions, the cross section is found to depend on the relative energies of

²³ D. Boyd, Ph.D. thesis, Rutgers University, 1968 (unpublished); available from University Microfilms, Ann Arbor, Mich.

²⁴ P. A. Assimakopoulos, N. H. Gangas, and S. Kossionides, Nucl. Phys. **81**, 308 (1965).

²⁵ G. G. Ohlsen, Nucl. Instr. Methods **37**, 501 (1965).

²⁶ Č. Zupančič, Nuclear Institute "J. Stefan" Report No. R-429, 1964 (unpublished); in *Few Nucleon Problems*, edited by Cerineo (Federal Nuclear Energy Commission of Yugoslavia, Hercegovina, 1964).

²⁷ J. V. Kane (private communication).

pairs of final-state particles. This relationship appears to be independent of momentum-transfer variables which characterize production amplitudes. We are thus led to hypothesize that such reactions are of a sequential form, consisting of a primary interaction or production process followed by final-state interactions between pairs of particles. To the extent that these steps are independent, we may study them separately by varying the relative-energy and momentum-transfer variables.

Final-state interaction theory depends on the assumption of successive independent interactions. This assumption is valid if the lifetime of the final-state two-particle system is sufficiently long for its decay not to be influenced by the presence of the third particle. In reactions involving nucleons, the 1S_0 interaction of two nucleons can produce a virtual state that approximately satisfies this requirement. Such a state is not a Breit-Wigner type of resonance and is not an exponentially decaying state. However, the 1s_0 phase shift has a rapid increase at about 70-keV relative p - n energy. A rapidly increasing phase shift may be interpreted as a time delay,^{28, 29} and the lifetime may be so defined. This leads to a pole in the scattering amplitude for such states, having the form $(k+i/a)^{-1}$, where k is the relative wave number of the two interacting nucleons, and a is the scattering length of the effective-range theory.³⁰ Since this expression has a maximum at zero relative energy, the interaction is sometimes referred to as a zero-energy resonance.

Watson³ showed that under certain conditions the matrix element describing a three-body breakup reaction could be factored into two parts: An amplitude describing the production mechanism, and the square of the relative wave function of the interacting pair $\psi(k, r)$ averaged over the production region. If this wave function is normalized to unity for zero interaction, then it becomes an enhancement factor for the production process. Fermi³¹ suggested a suitable normalized enhancement factor to be the square of the ratio of the wave function $\psi(k, r)$ to the wave function corresponding to zero phase shift, the ratio being evaluated at a radius corresponding to the range of the interaction. If we use the asymptotic wave function for s -wave continuum states and the effective-range theory, the enhancement factor E for an n - n or n - p final-state interaction is

$$E = \left| \frac{\psi(k, r_0)}{\psi^{(0)}(k, r_0)} \right|^2 = \frac{(1/r_0 - 1/a + \frac{1}{2}r_0k^2)^2}{k^2 + (1/a - \frac{1}{2}r_0k^2)^2}, \quad (2)$$

where r_0 is the effective range, a is the scattering length, and k is the relative wave number.

²⁸ M. L. Goldberger and K. M. Watson, *Collision Theory* (John Wiley & Sons, Inc., New York, 1964), p. 479.

²⁹ L. Eisenbud, Ph. D. thesis, Princeton University, 1948 (unpublished).

³⁰ For a discussion of effective-range theory, see S. De Benedetti, *Nuclear Interactions* (John Wiley & Sons, Inc., New York, 1964), p. 159.

³¹ E. Fermi, *Elementary Particles* (Yale University Press, New Haven, Conn., 1951), p. 58-64.

A consideration of the Coulomb repulsion yields the following expression for the p - p enhancement E_{pp} ³²:

$$E_{pp} = \frac{[1/r_0 - 1/a + \frac{1}{2}r_0k^2 - (1/\rho)h(\eta)]^2}{C^2k^2 + (1/C^2)[1/a - \frac{1}{2}r_0k^2 + (1/\rho)h(\eta)]^2}, \quad (3)$$

where

$$C^2 = 2\pi\eta/(e^{2\pi\eta} - 1), \quad \eta = e^2/\hbar v,$$

$\rho = \hbar^2/mc^2$, and $h(\eta)$ is a function evaluated in Jackson and Blatt.³³ m and e are the mass and charge of the proton, and v is the relative p - p velocity.

The presence of three strongly interacting particles in the $p+p+n$ system complicates the theoretical treatment considerably. If all three particles are in relative s states, they may all interact simultaneously. The symmetrization principle requires that we add the amplitudes for each simultaneous interaction, and in squaring, cross terms would arise that affect the cross section. In the case that only two particles interact strongly, we must add the amplitudes for the various pairwise interactions either coherently or incoherently, depending on whether the experiment can distinguish which pair interacted. The identity of the two protons tends to lower this distinguishability, and the requirement of fermion symmetrization can lead to experimentally observable effects in the cross section. Interference resulting from the identity of final-state particles has been reported by Phillips³⁴ in the reaction $B^{11}(p, 2\alpha)\alpha$.

The enhancement is given by the relative wave function of the interacting pair; it is therefore proportional to the probability that the two particles will be found at a small separation distance. In the independent pair model, it is assumed that these probabilities are dynamically independent for each pair. Therefore, according to this model, we should use a multiplicative enhancement factor

$$|\psi_{34}|^2 |\psi_{35}|^2 |\psi_{45}|^2.$$

Kinematically, the interactions are coupled by momentum and energy conservation. For example, if one pair has low relative momentum, then the third particle must have a large momentum relative to that pair, unless the center-of-mass energy is very low.

If the regions of two simultaneous enhancements are well separated, the multiplicative enhancement factor approaches the additive form, but if the enhanced regions overlap, this is not the case. If there are two overlapping resonances, the multiplicative form gives a more dramatic enhancement than the additive form. Present final-state interaction theory provides no general guides regarding the use of multiplicative or additive forms. This choice appears to be model-

³² Č. Zupančič, *Rev. Mod. Phys.* **37**, 332 (1965), and Ref. 65.

³³ J. D. Jackson and J. M. Blatt, *Rev. Mod. Phys.* **22**, 77 (1950).

³⁴ G. Phillips, *Rev. Mod. Phys.* **37**, 414 (1965).

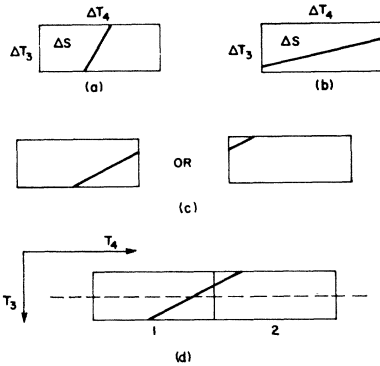


FIG. 2. (a), (b), (c). Three possible intersections of a kinematic line with a two-dimensional energy channel. (d) Treatment of case *c* by the computer program (see Sec. I E).

dependent. The Lee³⁵ and Khuri-Treiman³⁶ models lead to a product form of enhancement in the limit of two particles resonating with an infinitely massive third. References to other efforts concerning these problems are found in an article by Peierls and Tarski.³⁷ The theoretical answer to these questions may lie in the solution of the three-particle Lippmann-Schwinger equation, as in the work of Faddeev,³⁸ who showed that the series solution to the Lippmann-Schwinger equation could be reordered in terms of the two-body scattering amplitudes as follows:

$$T = T_0 + \sum_{\alpha} T_{\alpha} G_0 T_0 + \sum_{\alpha \neq \beta} T_{\alpha} G_0 T_{\beta} G_0 T_0 + \text{higher-order terms,}$$

where T_0 is the production amplitude, the T_k are the final-state pair amplitudes, and G_0 is the Green's function of the unperturbed Hamiltonian. The second term on the right-hand side corresponds to the diagrams of Fig. 1, which are discussed in Sec. I D, and the third term represents multiple final-state interactions. Aaron and Amado³⁹ have applied this formulation using s -wave, separable, spin-dependent two-body potentials. They were able to reproduce the major features of the $n+d$ data of Ilakovac *et al.*⁴ However, their theory predicts too narrow a final-state interaction peak. These calculations involve much of the full complexity of the three-body problem, but by means of judicious approximations, various applications to final-state interaction theory are beginning to emerge. Delbourgo⁴⁰ has obtained an amplitude that allows for interference between various final-state interactions, as well as inter-

ference with the production term:

$$T_{ba} = T_{bc}^{(0)} \left(1 + \sum_{i \neq j} C_{ij}(k_{ij}) \frac{\exp(i\delta_{ij}) \sin\delta_{ij}}{k_{ij}} \right).$$

The C_{ij} measure the strength of the i, j scattering relative to the unenhanced production term $T_{ba}^{(0)}$. In the limit of a single strong final-state interaction, this reduces to the simple Watson formula, Eq. (2).

D. Single-Interaction Model

Some special features of the $p+p+n$ final state at moderate energies suggest a simple model to treat possible multiple interactions. Since the characteristic dimensions of the deuteron are large, it is unlikely that all the pairs of particles will be in relative s states. Thus it is probable that if one proton is in an s state relative to the neutron, then the other proton-neutron pair is in a p state. Since there are no known p -state resonances in the nucleon-nucleon system, we might expect to have final states with only one interacting pair most of the time.

Neglecting the possibility of spin-flip processes, the possible final-state interactions may be represented by the diagrams of Fig. 1. The large circles represent a primary interaction that produces two particles in a relative s state. The small circles represent the final-state interactions of the two s -state particles. Since the spin of the three outgoing particles could be experimentally measured, final states with different spins should be regarded as distinguishable, and those with the same spins as indistinguishable. Therefore, the cross section should consist of a coherent sum of the indistinguishable diagrams and an incoherent sum of the distinguishable ones. If one studies the singlet final-state interaction of particles 3 and 5 (5 refers to the neutron), interference effects due to the indistinguishability of this diagram from those of the 3-4 singlet and the 4-5 triplet diagrams will occur.

Assuming a constant production mechanism represented by C_{ij}^k , a complex number, the amplitude for each diagram may be written as

$$C_{ij}^k \psi_{ij}^k = c_{ij}^k / (k_{ij} + i\alpha_{ij}^k),$$

where $q_{ij}^k = 1/a$, the inverse of the scattering length for particles i and j in the spin state denoted by k . The matrix element is

$$|M|^2 = |C_{35}^s \psi_{35}^s + C_{34}^t \psi_{34}^t + C_{45}^t \psi_{45}^t|^2 + \sum_{\text{other diagrams}} |C_{ij}^k \psi_{ij}^k|^2.$$

As will be discussed in Sec. II A, in coincidence measurements it is possible to select measuring conditions such that in the region of the 3, 5 resonance, where k_{35} is nearly zero and rapidly varying, k_{34} and k_{45} (and therefore ψ_{34} and ψ_{45}) are slowly varying and approximately equal. $|M|^2$ thus takes the form of interference of a

³⁵ R. W. Amado, Phys. Rev. **122**, 696 (1961).

³⁶ I. J. R. Aitchison, Nuovo Cimento (1964).

³⁷ R. F. Peierls and J. Tarski, Phys. Rev. **129**, 981 (1963).

³⁸ L. D. Faddeev, Zh. Eksperim. i Teor. Fiz. **39**, 1459 (1960) [Soviet Phys.—JETP **12**, 1014 (1961)]; Dokl. Akad. Nauk SSSR **138**, 565 (1961); **145**, 301 (1962) [English transl.: Soviet Phys.—Dokl. **6**, 384 (1961); **7**, 600 (1963)].

³⁹ R. Aaron and R. D. Amado, Phys. Rev. **150**, 857 (1966).

⁴⁰ R. Delbourgo, Nucl. Phys. **38**, 249 (1962).

resonant term with a constant background.⁴¹ It then follows that

$$|M|^2 = |C_{35}^s \psi_{35}^s|^2 (1 + C_{\text{int}} k_{35}) + \sum_{\substack{\text{all except} \\ i,j,k=3,5,s}} |C_{ij}^k \psi_{ij}^k|^2, \quad (4)$$

where

$$C_{\text{int}} = 2 \operatorname{Re} \{ C_{34}^s + C_{45}^t \} / k_{34}.$$

This matrix element describes a singlet p - n peak whose width is distorted from the simple Watson shape by an amount that depends on C_{int} . Thus, if C_{int} is not negligible, the simple Watson theory would lead to the extraction of the wrong scattering length. Although we can experimentally determine $|C_{34}^s|^2$ and $|C_{45}^t|^2$, their phase, and hence the value of C_{int} , could be predicted only by a more complete three-body theory. The analysis of the experimental peak could thus be interpreted as a measurement of the parameter C_{int} , rather than a measurement of a_{pn}^s , since a_{pn}^s is accurately known from elastic scattering.

In summary, since C_{int} increases as k_{31} (or k_{45}) is lowered, our model predicts the width distortion to increase with decreasing total center-of-mass energy. This indicates that studies of interference effects would be most sensitive at low incident energies, while extraction of two-body parameters from measured three-body cross sections would be most accurate at high energies. An additional result of this model is that, so long as C_{int} is small, the final-state interactions may be described by a sum of enhancement factors, one for each diagram of Fig. 1. This approximation is used in fitting our data and is described in more detail in Sec. IV E.

E. Phase Space

In many experiments, the three-body cross section is observed to be well reproduced by a phase-space distribution of events. This phase-space prediction is based on the assumption of a uniform population of events along the energy-momentum shell, and departures from such a distribution are considered to be the interesting features of the reaction. The differential phase space for a kinematically complete experiment is

$$\rho_1(T_3) dT_3 d\Omega_3 d\Omega_4 = \frac{P_3 P_4 dT_3 d\Omega_3 d\Omega_4}{1 + dT_3/dT_4}. \quad (5)$$

This form is not very useful, since it does not take into account the fact that the experiment deals with rectangular channels in T_3 and T_4 . In fact, $\rho_1(T_3)$ diverges where the kinematic line is tangent to the T_4 axis. What is needed is an expression for the phase space inside each rectangular $dT_3 \times dT_4$ channel. To do this, we need the expression for the phase space as a function of the arc length along the kinematic locus. The element of arc ds is given by the relation:

$$ds = [1 + (\partial T_4 / \partial T_3)^2]^{1/2} dT_3;$$

⁴¹ R. J. N. Phillips, Nucl. Phys. **31**, 643 (1962).

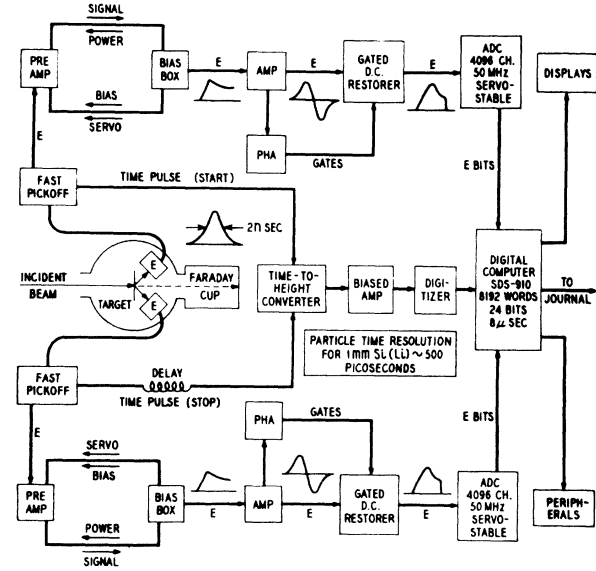


FIG. 3. Block diagram of the experimental electronics.

solving this for dT_3 and substituting into Eq. (5), we find that the expression for ρ_2 , the phase space per unit arc length, is given simply by

$$\rho_2(T_3, T_4) = \frac{\rho_1(T_3)}{[1 + (\partial T_4 / \partial T_3)^2]^{1/2}}.$$

The number of events falling into a certain channel which contains an element of kinematic line is proportional to

$$\int \rho_2(T_3, T_4) d\Omega_3 d\Omega_4 ds = \int \frac{P_3 P_4 d\Omega_3 d\Omega_4 ds}{[1 + dT_3/dT_4][1 + (\partial T_4 / \partial T_3)^2]}.$$

To evaluate this integral, we assume that the segment of kinematic line in each channel is straight, as shown in the diagrams of Fig. 2.

Case A.

$$\partial T_3 / \partial T_4 \geq \Delta T_3 / \Delta T_4 \quad [\text{see Fig. 2(a)}];$$

$$\Delta s = [1 + (\partial T_4 / \partial T_3)^2]^{1/2} \Delta T_3.$$

ΔT_3 and ΔT_4 refer to the actual widths of the experimental T_3 and T_4 channels, and $\Delta\Omega_3$ and $\Delta\Omega_4$ are the angular apertures of the detectors at θ_3 and θ_4 . We assume that ρ_2 is reasonably constant over the dimensions of a channel. The result is

$$\int \rho_2(T_3, T_4) d\Omega_3 d\Omega_4 ds = \frac{P_3 P_4 \Delta\Omega_3 \Delta\Omega_4 \Delta T_3}{1 + \partial T_3 / \partial T_4}.$$

Case B.

$$\partial T_3 / \partial T_4 < \Delta T_3 / \Delta T_4 \quad [\text{see Fig. 2(b)}];$$

$$\Delta s = [1 + (\partial T_3 / \partial T_4)^2]^{1/2} \Delta T_4,$$

$$\int \rho_2(T_3, T_4) d\Omega_3 d\Omega_4 ds = \frac{P_3 P_4 \Delta\Omega_3 \Delta\Omega_4 [1 + (\partial T_3 / \partial T_4)^2] \Delta T_4}{(1 + dT_3/dT_4)[1 + (\partial T_4 / \partial T_3)^2]}.$$

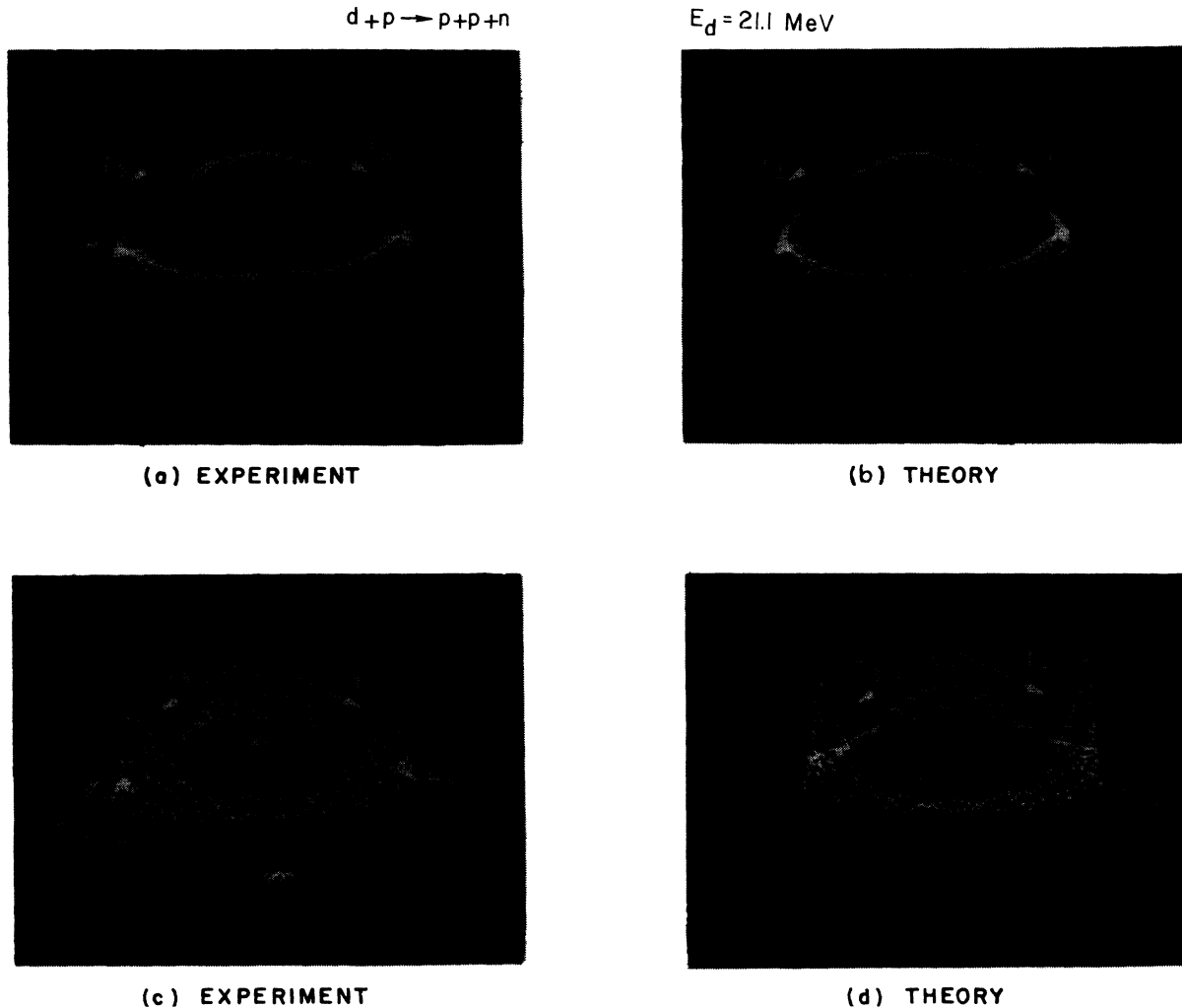


FIG. 4. Comparison of $d + p$ 21.1-MeV data with a complete simulation. *a* and *b* are at low count gain, and *c* and *d* at a higher count gain (see text).

Interchanging T_3 and T_4 according to the relation

$$[1 + \partial T_5 / \partial T_3] dT_3 + [1 + \partial T_5 / \partial T_4] dT_4 = 0,$$

this expression becomes

$$\int \rho_2(T_3, T_4) d\Omega_3 d\Omega_4 ds = \frac{P_3 P_4 \Delta\Omega_3 \Delta\Omega_4 \Delta T_4}{1 + \partial T_5 / \partial T_3}.$$

Case C. [See Fig. 2(c).] The cases shown in Fig. 2(c) cannot be treated explicitly by the above equations, but can be treated by using the following procedure to compute phase space. Consider the following example, in which the kinematic line crosses the two channels labeled 1 and 2 in Fig. 2(d). As described in the Appendix, the computer program steps down the T_3 axis channel by channel and searches for kinematic solutions in the center of each channel along the dashed line in the diagram. The program will find a solution in channel 1 but not in channel 2. However, the

Δs , which is computed according to case A above, includes both the parts that fall in channels 1 and 2. Thus, the contribution that falls into channel 2 will be added to the phase-space probability of channel 1. This procedure can never result in an error of more than $\frac{1}{2}$ channel and is usually much more accurate than that. If the experimental kinematic line is at least a few channels broad, such effects will cancel out.

Finally, from three-body kinematics we can obtain the result that

$$\partial T_5 / \partial T_4 = -\mathbf{V}_4 \cdot \mathbf{V}_5 / V_4^2,$$

or, relativistically,

$$\partial T_5 / \partial T_4 = (E_4 / E_5) \mathbf{P}_4 \cdot \mathbf{P}_5 / P_4^2.$$

The relations derived above are used in Monte Carlo calculations, which simulate our experimental data.

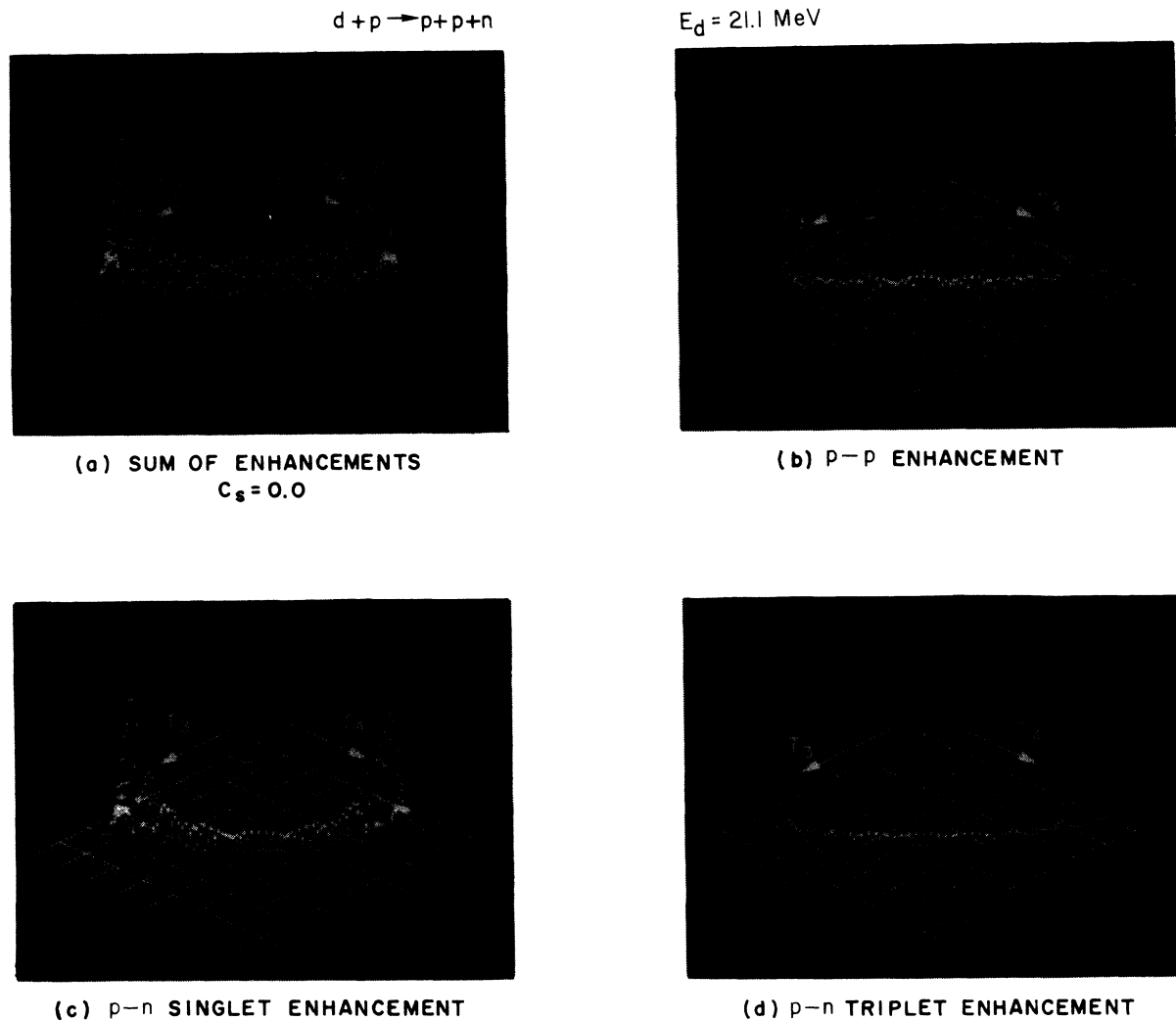


FIG. 5. Simulations using various enhancement factors for the $d+p$ reaction at 21.1 MeV in (b), (c), and (d); their sum in (a).

II. COINCIDENCE METHOD AND DATA SIMULATION

A. Advantages of Coincidence Experiments

The majority of previous investigations of nucleon-nucleon final-state interactions have consisted of measurements of the energy spectrum of one particle. If there is a final-state interaction with the two interacting particles having low relative energy, there will be a peak at the high-energy end of the spectrum of the other particle. The detector is usually placed at a forward angle because it is often experimentally observed that this high-energy peak is strongest there. In the breakup of a three-body system with high internal energy, the various relative momenta are free to assume a large range of values. A "singles" experiment, as described above, integrates over all of these momenta, and it is often not a good approximation to neglect the

intensity variation of the production process over the energy region of interest; that is, the primary interaction cannot be approximated by a phase-space distribution. In addition, final-state interactions between other pairs of particles are likely to occur, and these may distort the shape of the high-energy peak.

In coincidence measurements, the final-state interaction manifests itself by intensity modulation along the three-body locus in the two-dimensional energy spectrum. The additional kinematic constraints provided by the coincidence geometry permit the placement of the final-state interaction peak in a region of this locus where the production processes do not produce intensity modulation. Thus, it is reasonable to expect that the background under such a final-state interaction peak is essentially constant; the peak, therefore, should be well described by a final-state interaction enhancement of phase space.

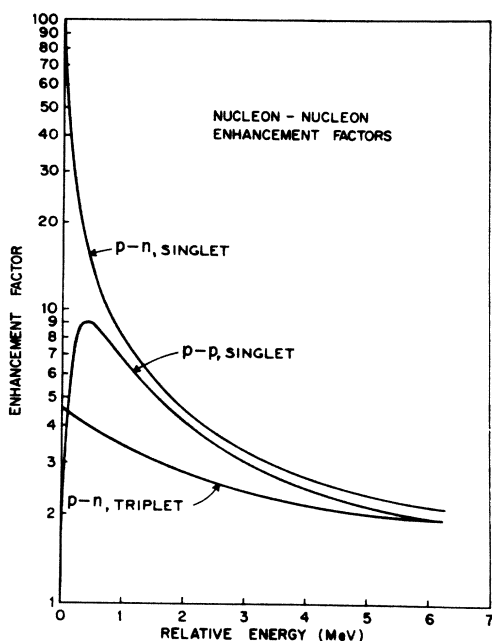


FIG. 6. Nucleon-nucleon enhancement factors for singlet and triplet spin states as a function of relative energy.

A further advantage of coincidence experiments is that three-body kinematics restrict the range of relative energies accessible to the various pairs of particles. This makes it possible to limit the contributions from other resonances, since, if the relative energy of one pair is selected to be small, then the others are, in general, large. In a singles measurement, the relative energies are not as severely restricted, even in the high-energy portion of the spectrum.

In our coincidence experiments on reactions of the type $1+2 \rightarrow 3+4+5$, we detect two particles at fixed angles. By our convention, they are particles 3 and 4 at angles θ_3 and θ_4 . If we wish to study a final-state interaction between particles 3 and 5, we choose the angles θ_3 and θ_4 to be those of the two-body reaction $1+2 \rightarrow (3,5)+4$. For example, in the reaction $p+d \rightarrow p+p+n$, the singlet deuteron (d^1) may be formed as an intermediate "state." Thus, $d^3+p \rightarrow d^1+p \rightarrow p+p+n$; $Q = -2.226$ and d^1 is the (3,5) system.

At these angles, the internal energy of the (3,5) system $T_{35 \text{ rel}}$ goes to zero at the point on the kinematic locus where T_4 is at a maximum. At this point T_3 is also equal to T_5 . As mentioned above, $T_{4,5 \text{ rel}}$ and $T_{3,4 \text{ rel}}$ will be large under these conditions; thus, we expect that final-state effects will not be important for pairs (3,4) and (4,5). In addition, since the different resonances are separated in energy, the possibility of interference between the various final-state interactions is decreased.

B. Data Simulation

In order to extract the p - n scattering length from our experimental data, we must somehow analyze the

broadened shape of the experimental p - n final-state interaction peak. The experimental broadening arises from the following sources: finite angular apertures of the detectors, finite beam-spot diameter, effects of target thickness, detector energy resolution and dead layer, and multiple scattering in the target. Although the contribution of each of these separate processes can be accurately calculated, great difficulties arise when one tries to unfold these effects from the data.

A possible method of attack is to fold into the projected theoretical spectrum a Gaussian function of some estimated appropriate width and to compare this with projections of the two-dimensional data onto either energy axis. However, much of the useful information measured in the experiment is lost when the two-dimensional data are projected. A refinement of the projection technique is to express the data and theory as a function of s , the length along the kinematic locus.⁴² This method reduces the errors that occur in regions where the kinematic line is nearly perpendicular to the energy axes. However, many comparison difficulties still remain; for example, the fact that the resolution function will vary with the curvature of the kinematic locus must be taken into account. Also, it must be borne in mind that the resolution function is not in general a Gaussian function.

All these problems are solved by the technique of "data simulation."^{43,44} In this method, the data are simulated by performing a Monte Carlo computer calculation. The simulation program accepts as input all factors relating to the experimental detector, target, and beam geometry, and parameters that describe target thickness and detector energy resolution. The program then calculates $\rho(T_3, T_4)$, the predicted energy distribution of events for a given experiment. Mathematically, this consists of evaluating the following integral:

$$\rho(T_3, T_4) = \iiint \frac{d^4\sigma}{d\Omega_3 d\Omega_4 dT_3 dT_4} \times R_3(T_3, T_3') R_4(T_4, T_4') d\Omega_3 d\Omega_4 dT_3' dT_4', \quad (6)$$

where $d^4\sigma/d\Omega_3 d\Omega_4 dT_3 dT_4$ is a theoretical differential cross section and $R_i(T_i, T_i')$ describes energy-resolution effects that arise from target thickness and energy resolution of the detectors. The angular part of this integral is computed by a Monte Carlo method. Random points are selected that lie within the experimental dimensions of the detectors and target beam spot. From these points the relevant particle energies are calculated. The integrand is then evaluated at each set of angles for each kinematically allowed T_3 and T_4 channel; the average of a large number of such computations multiplied by $\Delta\Omega_3 \Delta\Omega_4$ converges to the value of the angular part of the integral. In the calculations presented in this

⁴² P. A. Assimakopoulos and N. H. Gangas, Nucl. Instr. Methods **47**, 260 (1967).

⁴³ J. F. Mollenauer, IEEE Trans. Nucl. Sci. **NS-11**, 338 (1964).

⁴⁴ P. F. Donovan, Rev. Mod. Phys. **37**, 503 (1965).

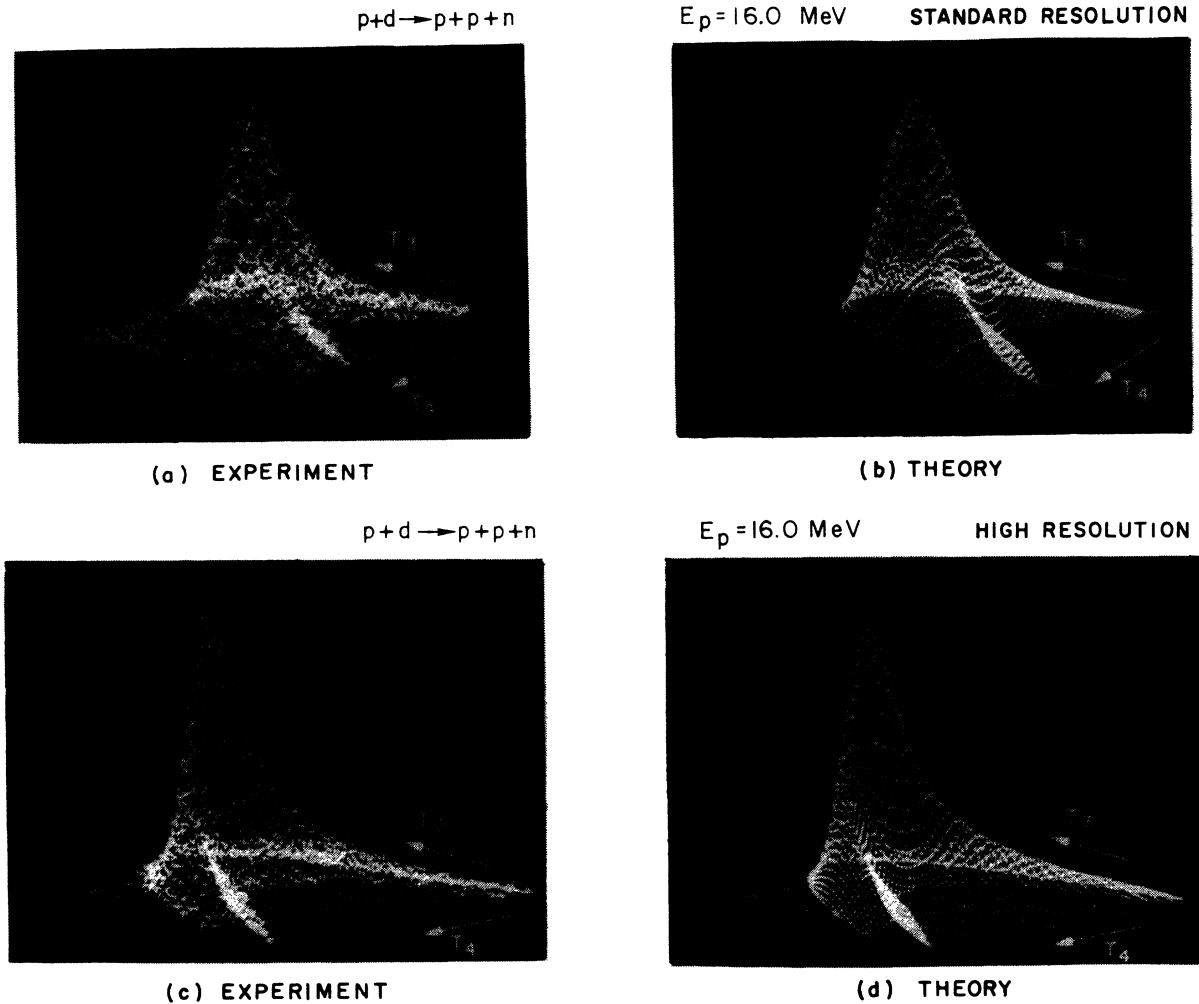


FIG. 7. Comparison of the $p+d$ 16-MeV data with theory. In (a) and (b) angular widths of the detectors were 2° . In (c) and (d) these widths were set to 1.4° in order to increase the resolution of the experiment. The resulting FSI peak is much narrower than its counterpart in (a) and (b).

work, the size of the T_3, T_4 energy array is 64×64 channels. The integration over T_3' and T_4' could be performed by selecting random energies along with the random angles. However, when the number of kinematically allowed channels in the simulated two-dimensional spectrum is large (≥ 500), the required computer time becomes significant. For this reason, the energy part of the integral is performed independently after the angular integration is completed. It was ascertained that this had no noticeable effect on the results.

The resolution function $R_i(T_i, T_i')$ consists of a product of two terms, one of which describes the energy loss of the detected particles in the target, and the other a Gaussian function which describes the energy resolution of the detectors. These integrals are evaluated numerically by approximating $R_i(T_i, T_i')$ with a step function. The details of these calculations are given in the Appendix. The result of this process yields a dis-

tribution of events $\rho(T_3, T_4)$ in which the experimental broadening effects are simulated as accurately as their individual contribution is known, and in the same way that they contribute in the actual experiment. By subtracting these simulations from experimental data, one achieves an easy quantitative comparison of theory with experiment without resorting to projection; theoretical parameters may then be adjusted as sensitively as the quality of the data will allow. This process is discussed in Sec. IV F.

C. Absolute Cross Sections

A quantity of theoretical interest is the differential cross section $d^4\sigma$. We may make the approximation

$$\frac{d^4\sigma}{dT_3 dT_4 d\Omega_3 d\Omega_4} = \frac{\text{number of counts per channel}}{\Delta T_3 \Delta T_4 \Delta \Omega_3 \Delta \Omega_4 N_p n_t},$$

where N_p is the number of incident projectiles, n_t is the number of target nuclei in the target per unit volume, t is the target thickness, $\Delta\Omega_3$ and $\Delta\Omega_4$ are the detector solid angles, and ΔT_3 and ΔT_4 are the energy widths of a channel. This expression is valid only if there are no broadening effects. The effect of the finite solid angle and other factors is to broaden the kinematic line. The

result is that experimentally we see fewer counts per channel than can be expected under "ideal" conditions (those under which there are no broadening effects). To find the actual cross section, we may account for the broadening by calculating a "smearing factor" using the simulation program. This smearing factor $S(T_3, T_4)$ is equal to

$$S(T_3, T_4) = \frac{\text{number of counts per channel in "ideal" experiment}}{\text{number of counts per channel in actual experiment}}$$

Thus, the corrected differential cross section is

$$\frac{d^4\sigma}{dT_3 dT_4 d\Omega_3 d\Omega_4} = S(T_3, T_4) \frac{\text{number of counts per channel}}{\Delta T_3 \Delta T_4 \Delta\Omega_3 \Delta\Omega_4 N_p n t}$$

The smearing factor $S(T_3, T_4)$ is given by

$$S(T_3, T_4) = \frac{|M|^2 F_{p.s.} dT_3 dT_4 d\Omega_3 d\Omega_4}{\iiint |M|^2 F_{p.s.} R_3(T_3, T_3') R_4(T_4, T_4') dT_3' dT_4' d\Omega_3 d\Omega_4}$$

$F_{p.s.}$ is the phase space factor, and R_3 and R_4 are functions that describe the energy-broadening effects, as in Eq. (6). The integration in the denominator is performed over the experimental solid angles Ω_3 , Ω_4 and energy channel widths. But this integration is exactly what the Monte Carlo simulation program calculates. Thus, we may calculate $S(T_3, T_4)$ in the following way:

$$S(T_3, T_4) = \frac{\text{simulation of ideal experiment}}{\text{simulation of actual experiment}}$$

Often the form of $|M|^2$ is only approximately known. However, if the full simulation has approximately the same shape as the experimental spectrum, then we may assume that the $|M|^2$ used is adequate for obtaining $S(T_3, T_4)$.

III. EXPERIMENTAL APPARATUS AND PROCEDURES

A. Beam Alignment

The beam from the Rutgers-Bell FN tandem Van de Graaff accelerator⁴⁶ was focused through a 2-m-long collimation system consisting of three adjustable circular tantalum apertures followed by antiscattering baffles. Each collimator assembly contained a selection of collimators having diameters of 1.0, 1.5, 2.0, and 3.0 mm, which could be rotated into a fixed position in line with the beam axis. With the smallest collimators in position, it was possible to maintain a beam spot of 1.0 mm on target.

The collimators were initially aligned optically, by requiring that each aperture be centered on an axis that was level with the accelerator and aimed at the center of the switching magnet. This axis was defined by a

Wild⁴⁶ telescope permanently mounted behind the scattering chamber. As a final check on the alignment, a laser beam was directed through the eyepiece of the telescope. The laser beam was thus focused at the center of the switching magnet. The optical axis could then be located everywhere along the beam line by the insertion of a scale at the point of interest.

A calculation of the effect of the earth's magnetic field on our particle beams showed that this effect could produce a deflection of about 1 mm over the length of the collimation system. In order to reduce this effect, magnetic shielding metal was inserted in the beam pipe along a part of the collimation system. Even with this precaution, shifts of about 0.5 mm on the target were observed to occur with various beams. Such a shift can result in an angular missetting of the detectors of the order of $\frac{1}{2}^\circ$. Consequently, before each experiment, the scattering chamber was checked for left-ring angular symmetry, using a scattering angular distribution with a very sharp angular dependence.

Once the beam was switched into the beam line, it was focused into the scattering chamber with a magnetic quadrupole lens. It was found necessary to observe the beam just before it entered the first collimator in order to initially steer it into the scattering chamber. Therefore, at that point, a rare-earth-doped Pyrex glass fiber,⁴⁷ about 6 cm long and 0.2 cm in diameter, was rotated in the beam at a 45° angle. The glass fiber fluoresced brightly enough so that even very weak beams (less than 10^{-9} A) could be easily viewed with a TV monitor placed at 90° to the beam. This system has the advantage over the usual quartz viewer because it does not block the beam, and the beam current may be monitored farther downstream while the fiber is rotat-

⁴⁶ Manufactured by High Voltage Engineering Corp., Burlington, Mass.

⁴⁶ Wild Corporation, Heerbrugg, Switzerland.

⁴⁷ Obtained from H. Guggenheim, Bell Telephone Laboratories, Inc., Murray Hill, N. J.

TABLE I. Experimental parameters used in simulations.

Projectile	Protons	Deuterons	Deuterons	Deuterons
Beam energy (MeV)	16.0	21.1	16.0	10.0
θ_1 (deg)	-29.72	-26	-19.26	-30.37
θ_3 (deg)	82.55	26	41.27	15.87
φ_3 - φ_4 (deg)	180	180	180	180
Servo pulser (MeV)				
$P1(T_4)$, Ch64	8.9 ^a	15.75	7.89	3.27
$P2(T_4)$, Ch16	3.03	4.25	2.98	2.37
$P1(T_3)$, Ch64	4.79	15.75	4.91	4.0
$P2(T_3)$, Ch16	4.03	4.25	3.41	2.0
Detector resolution in channels				
T_4 FWHM	0.8	0	1	3
T_3 FWHM	5.1	0	3	2
Target angle (deg)	40	0	0	0
Target thickness (mg/cm ²)	2.3 ^a	2	1.05	0.3

^a In the high-resolution data shown in Figs. 7(c) and 7(d), $P1(T_4)$ was 8.0 and the target thickness was 0.5 mg/cm².

ing. Advantages of this system over beam scanners are complete beam shape determination, low cost, and simplicity of position calibration.

B. Scattering Chamber

The scattering chamber was 40 cm in diameter with a clear plastic top. Two detectors, one mounted on a circular plate and one on a movable arm, could be positioned from outside the chamber with a precision of 0.1°. By rotation of a turret mechanism mounted on the plastic top, any one of six targets could be lowered into the geometric center of the chamber. One of the target holders held a Pu²³⁹-Am²⁴¹ mixed source used for α -particle detector calibrations.

The Faraday cup was 1 m long, with a tantalum beam stop at the end; this beam stop could be rotated 90° to expose a quartz plate mounted at the end of the beam pipe, which was used for monitoring the beam position. The telescope, which was mounted directly behind the Faraday cup, could view the inside of the scattering chamber through this window. This was found useful for measuring the size and position of the beam spot on the target and for aligning the detector collimators.

C. Targets

The targets used in these experiments were polyethylene (CH₂) and deuterated polyethylene (CD₂) foils. Although a gas target cell was available, the advantages of using a thin foil far outweigh the disadvantage of having C¹² in the target. 1-mg/cm² CH₂ targets were cut from commercial polyethylene material of this density. Thinner targets were made by dissolving polyethylene and casting from hot xylene.^{48,49} CD₂ and

⁴⁸ G. I. J. Arnisson, Nucl. Instr. Methods **40**, 359 (1966).

⁴⁹ R. Klein (private communication).

CH₂ foils about 1 cm² in area and 0.1 mg/cm² thick were made with this method.

D. Electronics

The detectors used in the various measurements were either the lithium-drifted silicon p - n junction⁵⁰ type or the silicon surface-barrier type,⁵¹ with depletion regions 1–3-mm thick.

A block diagram of the electronics used in these experiments is shown in Fig. 3. The detector signals were amplified by charge-sensitive preamplifiers, using field-effect transistors (FET's). The amplified signals traveled through a signal-handling cable system⁵² to the control room, where they were further amplified with Tennelec⁵³ TC-200 amplifiers. The signals were then fed through gated dc restorers⁵⁴ and into two 50-MHz 4096-channel analog-to-digital converters⁵⁵ (ADC's). The ADC's were stabilized with two levels of precision pulses, which went to the preamplifier through the detector bias cable. These servo pulses then traveled through the electronics in the same way as detector pulses, back to the ADC's. The internal gain of the ADC's was varied in order to force the higher servo pulser to store in channel 4096, and the lower one in channel 1024. Therefore, both gain and zero intercept of the ADC's were servoed. The servo pulse heights were varied by precision potentiometers, which could be normalized to be direct reading in MeV. In order to

⁵⁰ Purchased from Technical Measurements Corp., San Mateo, Calif.

⁵¹ ORTEC, Oak Ridge, Tenn.

⁵² Designed by E. A. Gere, W. Gibson, and G. L. Miller, Bell Telephone Laboratories, Inc. Murray Hill, N. J.

⁵³ Tennelec, Oak Ridge, Tenn.

⁵⁴ E. A. Gere and G. L. Miller, IEEE Trans. Nucl. Sci. **NS-14**, 89 (1967).

⁵⁵ E. A. Gere and G. L. Miller, IEEE Trans. Nucl. Sci. **NS-13**, 508 (1966).

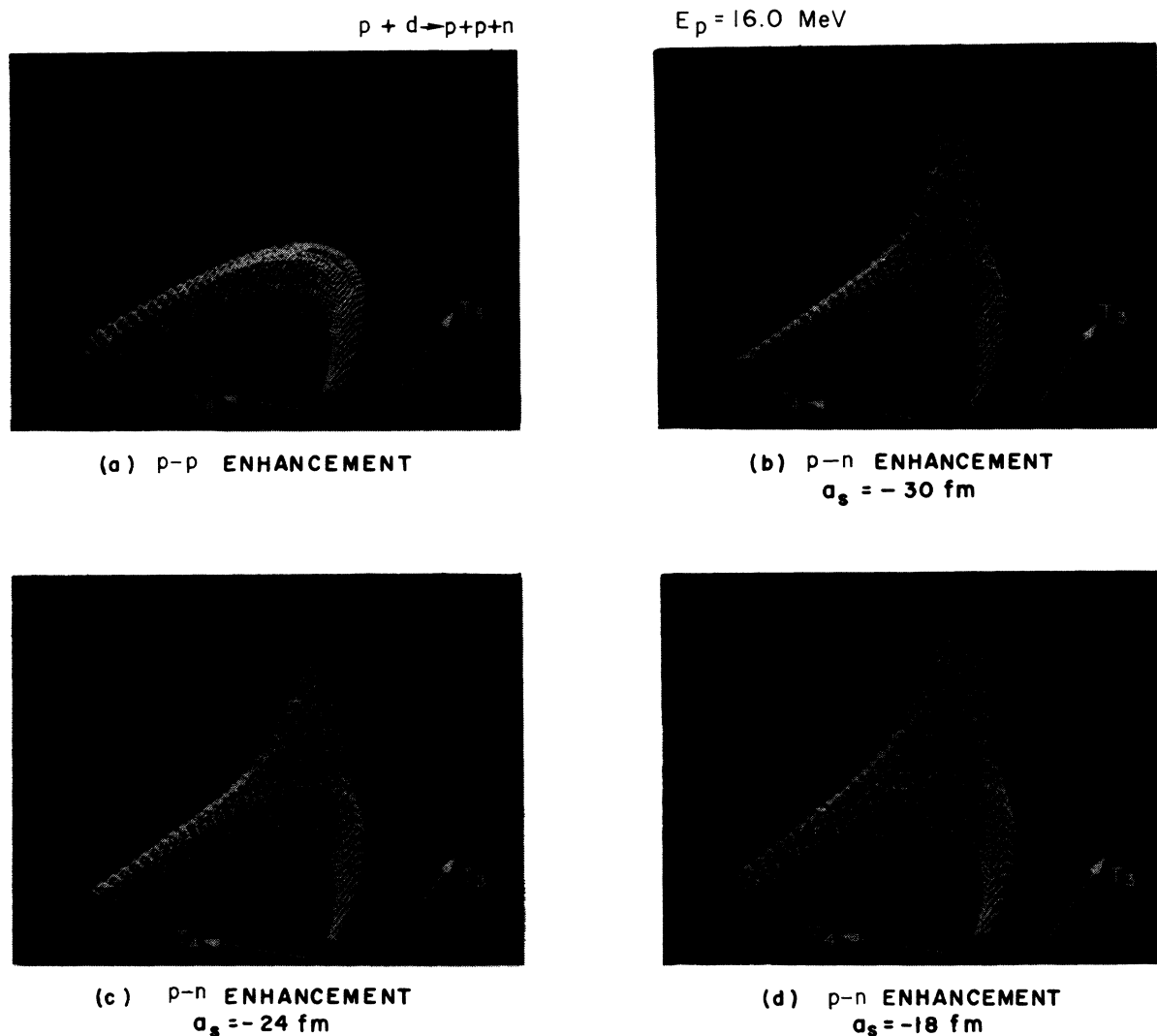


FIG. 8. Raw Monte Carlo simulations of the 16-MeV $p+d$ experiment without the smearing due to target thickness and detector energy resolution being folded in. The effect of varying the singlet $p-n$ scattering length for particles 4 and 5 is illustrated in (b), (c), and (d).

change the energy calibration precisely, the potentiometers were reset to the new values, and the external amplifier was adjusted so that the ADC's were in their servo range. If the lower pulser ($P2$) is adjusted to greater than $\frac{1}{4}$ of the upper one ($P1$), then channel 0 will be greater than 0 MeV, and the energy scale is expanded. This made the use of a biased amplifier unnecessary in achieving the greatly expanded energy scales used in these experiments.

Elastic deuterons or protons were scaled in order to make possible comparison of the experiments with absolute theoretical predictions, should any be forthcoming. Cosmic 801 discriminators⁵⁶ were used to set energy channels on the peaks that were scaled. The coincidence electronics consisted of Ortec⁵¹ 260 fast-

transformer-coupled pickoffs, which gated an E.G. & G.⁵⁷ time-to-amplitude converter.

E. Computer Techniques

The data were accumulated in an on-line SDS-910 computer⁵⁸ that had 8192 memory locations. The ADC's are interfaced⁵⁹ to the computer's 24-bit parallel-input connector (PIN) through a buffer register. When the buffer is ready, the interface sends an interrupt to the computer, which causes the program to branch from the display subroutine to the data-taking subroutine. This subroutine increments the memory location specified

⁵⁷ E. G. & G., Salem, Mass.

⁵⁸ Scientific Data Systems, Santa Monica, Calif.

⁵⁹ J. V. Kane, in *Proceedings of Scottish Universities, Fifth Summer School* (Plenum Press, Inc., New York, 1965).

⁵⁶ Cosmic Radiation Laboratories, Inc., Bellport, N. Y.

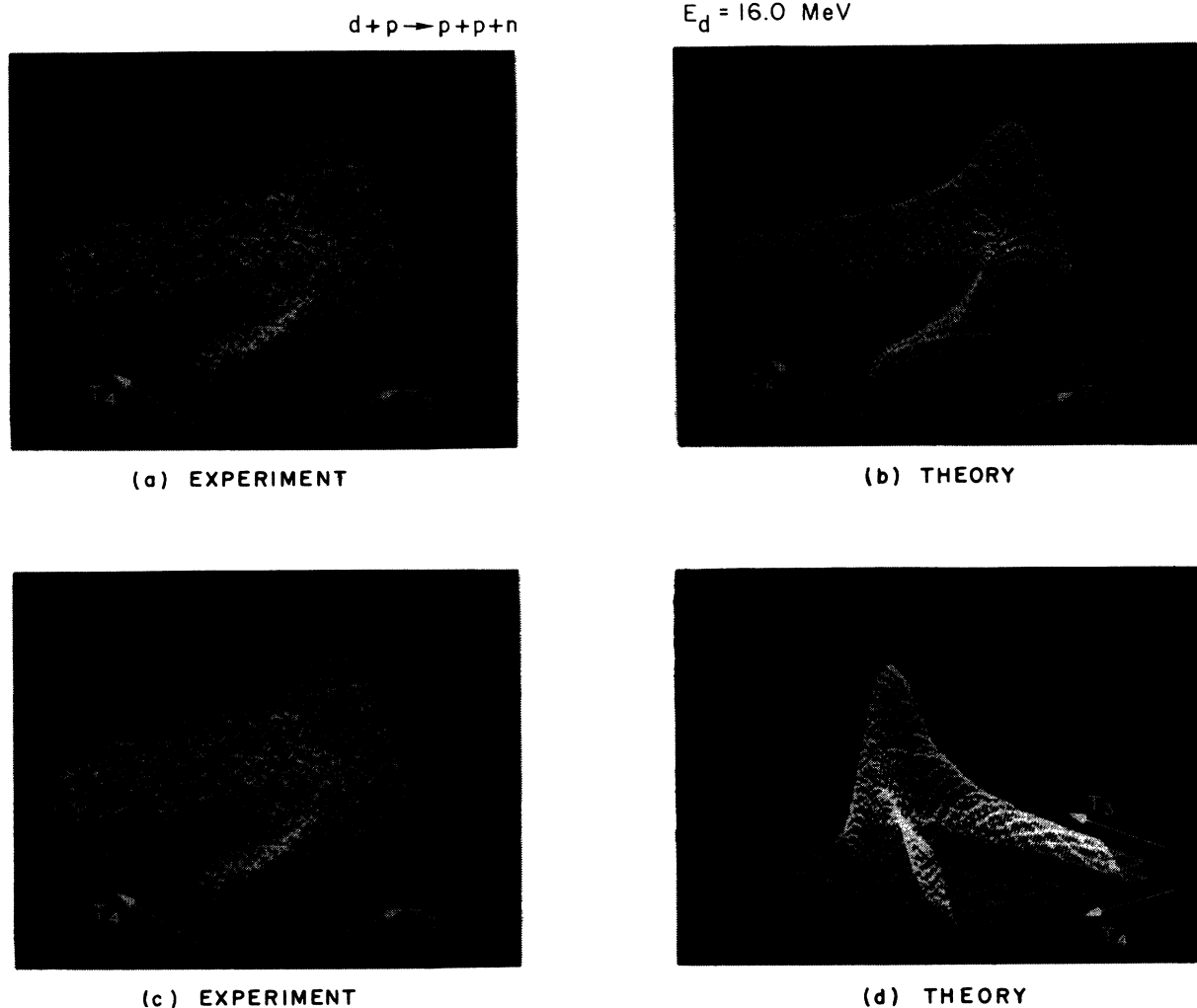


FIG. 9. Comparison of the $d+p$ 16-MeV data with theory from two perspectives.

by the binary number read in on the PIN connector. This binary number consists of six bits from the T3 ADC, six bits from the T4 ADC, and three bits from a third ADC, which digitizes the time-channel information.

Between data interrupts, a live three-dimensional display is generated by the display subroutine. A cathode-ray oscilloscope is driven by three digital-to-analog converters (DAC's). A rectangular channel grid is generated by the x and y DAC's, which derive their six bits each from the computer S register, which contains the memory address of the channel being displayed. The z DAC produces a vertical deflection of these grid points. The input to the z DAC is the parallel-output (POT) connector, which contains the number of counts in the channel being displayed. The x and y DAC outputs can be transformed by rotation about two axes through an angle θ by an analog display rotator. This produces an isometric display with various

degrees of tilt. Every eighth dot in the grid is brightened to facilitate the determination of channel numbers.

Since the two-dimensional data-taking program requires 6144 locations for data storage, it was written in assembler language in order to fit in the remaining 2048 memory locations. Therefore, the input-output capabilities of this program are limited. The normal output was via the paper-tape punch. Paper-tape dumps were found to be easier to catalog than the binary magnetic-tape dumps that the program can write. Since the coincidence runs were usually fairly long, the quantity of paper tape produced per unit time was not excessive.

F. Fast-Coincidence Techniques

The time at which a leading-edge discriminator fires depends on the pulse voltage, the detector rise time, and the particle arrival time. Each of these factors in turn depends on the particle energy. Therefore, the fast-

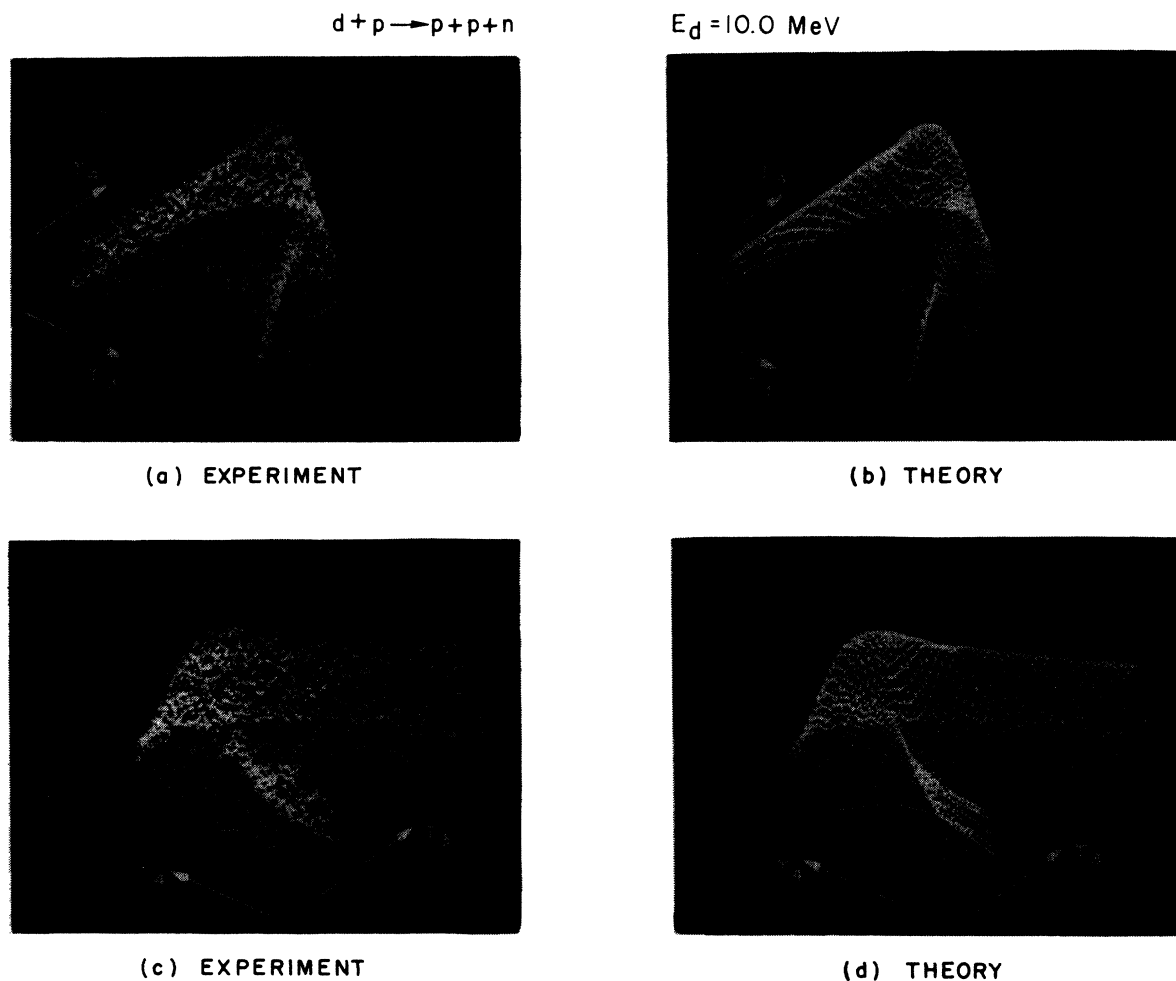


FIG. 10. Comparison of the $d+p$ 10-MeV data with theory.

coincidence signals have a time-energy correlation. To minimize this effect, the discriminator level should be set as low as possible, and the rise times of the detector pulses should be made as fast as possible. In order to trigger on pulses whose rise time was not degraded by the preamplifier, a transformer-coupled time pickoff⁶⁰ was placed in the circuit immediately after the detector and before the preamplifier.

In this configuration the rise time is limited by the charge-collection time and the CR time of the detectors. The charge-collection time depends on the detector bias and the penetration depth of the detected particles.⁶¹ For proton energies up to 12 MeV, a charge-collection time of about 30 nsec can be obtained by using 1-mm Si(Li) detectors run at 300–400 V bias. The detector CR time is only a few nsec. It is advantageous to have

a capacitance to ground, located after the time pickoff, which is greater than the detector capacitance. This optimizes the rise time of the current pulse going through the time pickoff. Usually about 3 ft of 50- Ω cable between the time pickoff and the preamplifier will satisfy this requirement.

With the above configuration, the resolving time between two detectors, which detect coincident 6-MeV monoenergetic protons, was found to be about 500-nsec full width at half-height. With an electronic pulser, a resolving time of about 350 psec was obtained. Thus, there is a broadening of the resolving time due to detector effects such as straggling of particle ranges in the detector and dispersion of charge-collection times.

There is a substantial variation in the triggering time of the pickoffs with particle energy, because of the time-energy correlation effects previously mentioned. This time-energy correlation, which is about 1 nsec per MeV for protons, can be compensated for by using techniques described below. It also often provides a

⁶⁰ C. W. Williams, W. E. Kiker, and H. W. Schmitt, *Rev. Sci. Instr.* **35**, 1116 (1964).

⁶¹ Blignant and McMurray, *Nucl. Instr. Methods* **51**, 102 (1967).

TABLE II. Extracted values of theoretical parameters.

Reaction	$p+d$	$d+p$	$d+p$	$d+p$
Beam energy (MeV)	16.0	21.1	16.0	10.0
c.m. energy (MeV)	8.44	4.81	3.11	1.11
T/S	2.0 ± 0.5	3.0 ± 0.5	3.0 ± 1	5.0 ± 2
C_{pp}	3 ± 2	3 ± 1	3 ± 2	5 ± 2
C_s	0 ± 0.3	1 ± 0.1	0.5 ± 0.3	0.5 ± 0.3
$-a_s$ (F)	23.8 ± 0.5	24 ± 4	23.5 ± 2	24 ± 6

convenient method of discrimination between different particle types.⁶²

The two fast signals from the time pickoffs were used to start and stop an E.G. & G. time-to-amplitude converter (TAC).⁵⁷ The output of the TAC is a pulse whose height is proportional to the time difference between the arrivals of the two fast signals. This pulse was amplified with an E.G. & G. biased amplifier⁵⁷ and then digitized. In the early experiments, a six-channel stacked discriminator was used for this purpose. More recently, a third ADC was used, as described in Sec. III E.

In the most recent version of the data-taking program, the computer memory is arranged in a three-dimensional array, $64 \times 64 \times 6$ channels. This is done by a word-splitting procedure that allows a channel depth of only 64 events. The two-particle energies are stored with a precision of 64 channels, and the time-difference information in six channels. The time-energy correlation corrections may be made off line after the experiment. In the reactions of interest here, the counting rate is high enough so that the experiment is self-calibrating; that is, in each of the six 64×64 T_3 - T_4 arrays, the coincident events quickly populate a bounded area or time zone. Since lines of constant time difference are straight lines radiating from the energy origin, we can easily estimate the energy region corresponding to real coincidences. In very low-rate experiments, or when the real-to-random ratio is low, the real coincidence energy regions can be determined by running a suitable high cross-section reaction as a timing calibration.

IV. DESCRIPTION AND ANALYSIS OF EXPERIMENTS

A. Analysis of Reaction $p(d, 2p)n$

Figures 4(a) and 4(c) are photographs of data obtained by Donovan, Kane, Mollenauer, and Zupančič⁶³ at Brookhaven, at 21.1-MeV incident deuteron energy. Zero energy for both protons is at the top corner of the

array, with the two-proton energies increasing in the directions shown by the arrows. In this form of display, regions of high cross section manifest themselves by upward displacement of the grid points. The data of Figs. 4(a) and 4(c) are identical; Fig. 4(c) has a higher count gain. The energy calibration of each proton axis is 12.0 MeV in channel 48. The data were taken with the detector angles at plus and minus 26° (coplanar on opposite sides of the beam axis), and the detector angular widths were 2.5° .

The most striking features of the data of Fig. 4 are the two pronounced peaks centered near channels (12, 48) and (48, 12), the strong ridge connecting these peaks, and the low-energy peak near channel (8, 8). An understanding of the origin of these peaks is facilitated by a consideration of the particle kinematics. In the region of channels (12, 48), the lower-energy proton has the same energy and direction as the undetected neutron. Hence, these two particles have zero relative momentum, and they may be expected to experience a strong final-state interaction. The resulting enhancements may be calculated with the Watson formula; simulations are shown in Figs. 4(b) and 4(d), which take into account both the singlet and triplet spin states. The triplet enhancement was multiplied by a factor of 3; this was necessary to fit the experimental data and represents a manifestation of the greater statistical weight of the triplet state.

In the region of the peak in channel (8, 8), the two protons have low laboratory energy, and hence low relative energy. We might then expect a peak due to a proton-proton final-state interaction. This enhancement is shown in Fig. 5(b). The simulated low-energy peak is considerably smaller than the peak that is observed experimentally [cf. Fig. 4(c)]. Figure 5(a) shows the sum of the enhancements given in Figs. 5(b)–5(d). Comparison with the data [Fig. 4(c)] shows that final-state interaction theory does not account for the magnitude of the low-energy peak, and we should therefore consider the primary interaction mechanism as a possible contributor.

Examining the kinematics, we find that in this region of the T_3 , T_4 array, the (unobserved) neutron travels forward with essentially the same momentum it had in the incident beam; the two protons, however, suffer a large momentum transfer. We thus are led to try a

⁶² P. Assimakopoulos, E. Beardsworth, D. P. Boyd, and P. F. Donovan, *Bull. Am. Phys. Soc.* **14**, 22 (1969).

⁶³ P. F. Donovan, J. F. Mollenauer, Č. Zupančič, D. Boyd, and P. D. Parker, in *Proceedings of International Conference on Nuclear Physics, Gallinburg, Tenn. 1966*, edited by R. L. Becher (Academic Press Inc., New York, 1967).

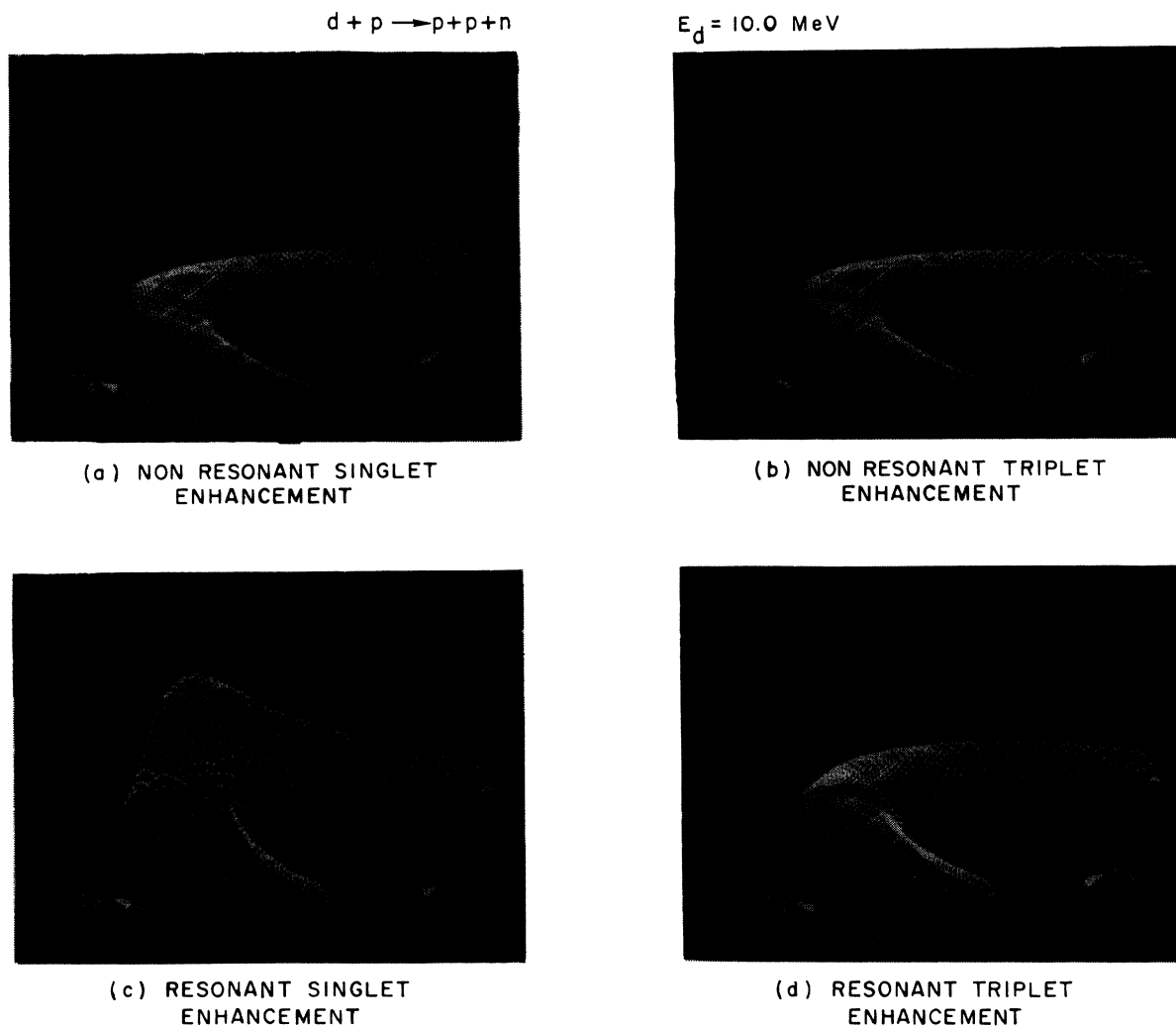


FIG. 11. (a) and (b). Singlet and triplet enhancement factors for the “nonresonant” particles 4 and 5. (c) and (d). The same enhancements for the “resonant” particles 3 and 5, which are formed with low relative energy.

simple knockout model,³² using the Born approximation. This model is sometimes called the “spectator” model; this term refers to a spectator particle, here the neutron, which does not participate in the collision. If we assume a Hulthén type of wave function for the deuteron, the amplitude for this process is⁶⁴

$$\psi(P_n) = (P_n^2 + \alpha^2)^{-1} - (P_n^2 + \beta^2)^{-1},$$

where P_n is the momentum transferred to the neutron in the collision; $\alpha/\beta = 1/7$; $\alpha^2 = -m_n B$, where $B = -2.226 \text{ MeV}$, the binding energy of the deuteron; and m_n is the neutron mass. A simple physical way of looking at this process is indicated by the fact that $|\psi(P_n)|^2$ is the probability distribution for the momentum of each particle in the deuteron. The reaction thus proceeds as a

⁶⁴ For the procedure used in the calculation of this amplitude, see P. F. Donovan, J. V. Kane, Č. Zupančič, C. P. Baker, and J. F. Mollenauer, Phys. Rev. **135** B75 (1964).

free two-body reaction, but with an initial velocity spread of the struck particles given by $|\psi(P_n)|^2$.

Figures 4(b) and (d) shows the result of multiplying Fig. 5(a) by this amplitude. Theory is now in quite good agreement with experiment. The success of this fit lends additional confidence in the form of the matrix elements that are used to extract the p - n scattering length in the higher-resolution experiments.

B. Higher-Resolution Experiments: Selection of Angles and Energies

In order to examine the fine details of the p - n final-state interaction, new experiments were undertaken. The energy axes of the two-dimensional spectrum were expanded so that one of the p - n final-state interaction peaks of Fig. 4 was spread out over a region encompassing about 1000 channels. The coincidence resolving time was improved by taking into account the time-

energy correlation of the detected particles. This made it possible to run at a higher counting rate without introducing an unacceptable number of random coincidences. Also, the solid angles of the detectors and the target thickness were reduced. These experimental improvements are described in detail below.

We wish to test final-state interaction theory and the effect of kinematic factors on its predictions. When a singlet deuteron is formed in the $p+d$ reaction, the singlet deuteron and the preparing proton emerge in opposite directions in the center-of-mass system. If we wish to vary the relative velocity between them, we must vary the center-of-mass energy of the reaction. This is given by

$$E_{c.m.} = [m_2 / (m_1 + m_2)] T_1 + Q, \quad Q = -2.226 \text{ MeV.}$$

As we go to higher center-of-mass energy, and thus higher relative velocity for the final-state particles, the interaction of the proton with the decaying singlet deuteron becomes smaller, and the assumptions of Watson theory become more valid. Such interfering effects can become quite important. For example, in the $d+p$ reaction at 10-MeV incident deuteron energy, the center-of-mass energy is only 1.1 MeV, and since the $p-p$ interaction is strongest at about 0.4-MeV relative energy (Fig. 6), one can expect an appreciable effect from this source regardless of any kinematic constraints imposed.

The $p+d$ and $d+p$ reactions were studied at center-of-mass energies of 1.11, 3.11, 4.81, and 8.44 MeV. At each incident energy, the laboratory angle of the two

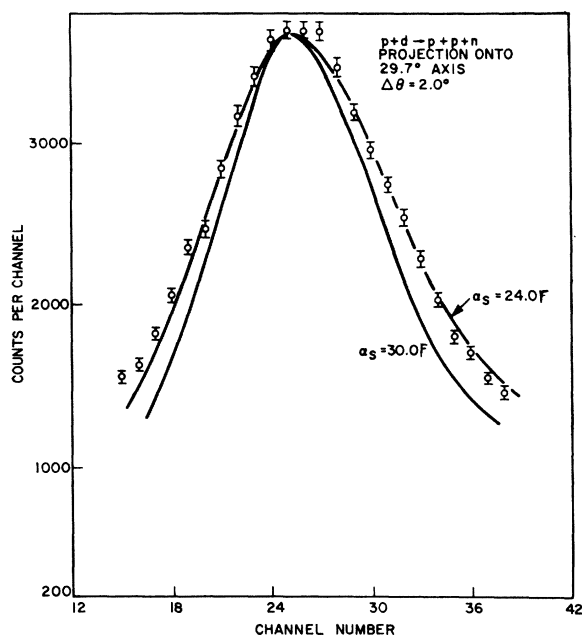


FIG. 12. Projection of the $p+d$ 16-MeV data (circles) and two simulations (solid curves) onto the T_4 axis. This illustrates the sensitivity to the scattering length in a projection treatment of the data.

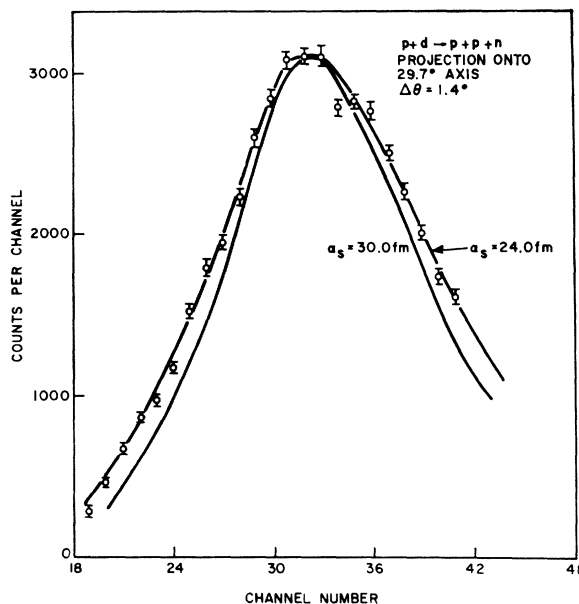


FIG. 13. Projection of the high-resolution $p+d$ 16-MeV data onto the T_4 axis.

protons was chosen so that they had approximately equal laboratory energies when singlet deuterons were formed. This ensured that the detected protons had a substantial laboratory energy (>3 MeV) over the region of interest. At such energies, the fast-pickoff time resolution is better than at lower energies, and the effects of target thickness and dead layers on the detectors are less important.

In addition, at these angles a “kinematic-amplifier” effect is observed. An investigation of the kinematics shows that when a decay particle is emitted by a system that has low excitation energy (just above the decay threshold) and high laboratory velocity, the laboratory kinetic energy of this decay particle is a very sensitive function of the system excitation energy; that is, $dT/dE^* \gg 1$, where T is the laboratory energy of the decay particle, and E^* is the energy above threshold of the decaying system.

In the $p-n$ final-state interaction peaks shown in the data of Figs. 4(a) and 4(c), one sees that the laboratory energy of the lower-energy (decay) proton varies by about 2 MeV across the peak; this region is only about 200 keV broad in the $p-n$ center-of-mass system. Therefore, we have a kinematic-amplification factor $\Delta T/\Delta E^*$ of about 10. This means that, in principle, we could see structure in the final-state interaction peak with a resolution about 10 times sharper than the detector resolution, or about 7 keV. This effect has been used to measure with otherwise unattainable precision the position and shape of particle-emitting states of He^4 .^{65,66}

⁶⁵ P. F. Donovan, Rev. Mod. Phys. **37**, 506 (1965).

⁶⁶ P. D. Parker, P. F. Donovan, J. V. Kane, and J. F. Molle-
nauer, Phys. Rev. Letters **14**, 15 (1965).

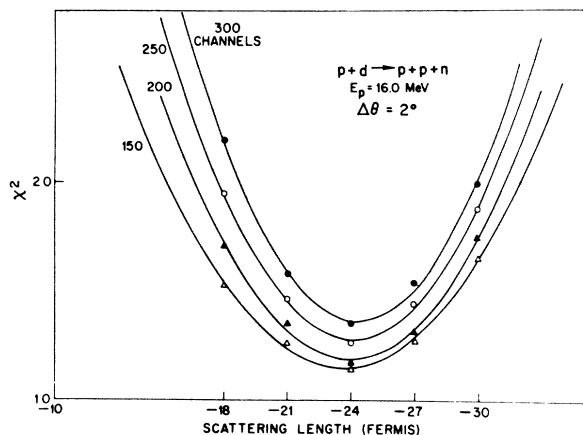


FIG. 14. χ^2 fits of selected regions of the 16-MeV $p+d$ final-state interaction peak to various scattering lengths. The ordinate is the normalized χ -squared deviation, and the abscissa is the singlet $p-n$ scattering length. Each of the four curves were computed using regions that encompassed channels from the peak maximum down to some level that was about $\frac{1}{3}$ -maximum for the largest area (300 channels) that is plotted.

The selection of detector solid angles depends on the choice of a real counting rate and a tolerable ratio of reals to randoms; these in turn depend on the coincidence and singles counting rates and on the experimental coincidence resolving time. A large solid angle is desirable in order to achieve high data accumulation rates; however, the energy spread associated with large angular apertures dictates that these be kept as small as practicable. In view of the necessary compromise involved, we selected for the high-resolution runs solid angles of $\Delta\Omega_3 = \Delta\Omega_4 = 4.06 \times 10^{-3}$ sr, and, in the case of the highest-angular-resolution experiment, $\Delta\Omega_3 = \Delta\Omega_4 = 2.03 \times 10^{-3}$ sr. These were defined by placing collimators 0.3 cm wide by 1.0 cm high at distances of 8.6 and 12.2 cm from the target. This corresponds to angular widths of 2° and 1.4° in the reaction plane. The rectangular shape of the collimators minimizes the energy dispersion due to $dE/d\theta$ in the experiment, since the relative angle between the detected protons varies less for a shift in φ (out of the reaction plane) than it varies with θ (in the reaction plane).

C. Description of Experiments

The experimental detector angles, bombarding energies, and energy calibrations of the high-resolution runs are summarized in Table I. In the first $p+d$ 16-MeV runs, in which $\Delta\theta$ was 2.0° [see Figs. 7(a) and 7(b)], 3-mm Si(Li) detectors were used, and a resolving time of 7 nsec was achieved; a 4-nA beam was maintained on a 2-mg/cm² CD₂ target for a period of 48 h, and about 200 counts per channel were accumulated in the singlet deuteron peak. 26.8×10^6 elastic protons were detected in the 82° detector. Many months later, this run was repeated at higher resolution, with $\Delta\theta = 1.4^\circ$

[see Figs. 7(c) and 7(d)]. In this run, the coincidence resolving time had been improved to 0.8 nsec due to the use of the coincidence circuit described in Sec. III F and the use of 1-mm-thick surface-barrier detectors. The beam current was 70 nA, the target thickness was 0.5 mg/cm², and 46.1×10^6 elastic protons were scaled in the 82° detector.

The 16-MeV $d+p$ experiment was run for 40 h at 0.5 nA on a 1.0-mg/cm² CH₂ target, and 23.2×10^6 elastic protons were scaled at 41.27° . With the old electronics, the resolving time was 7 nsec.

Surface barrier detectors, 0.5 mm thick, were used for the 10-MeV $d+p$ run. The beam current was 10 nA for 38 h and a 0.3-mg/cm² CH₂ target was used. 120.0×10^6 deuterons, which were scattered backward in the c.m. system, were scaled in the 15.9° detector. The coincidence resolving time was 1.5 nsec. The amount of beam current that could be used was limited by pileup in the 15.9° detector.

In all the runs, a random-coincidence spectrum was stored, and we could, in principle, subtract this spectrum from the data. However, this background was roughly uniform and of the order of one count per channel or less, and the interesting region of the real spectrum contained 100–300 counts per channel. Hence the accidental-coincidence correction was negligible, and no subtraction was made.

Full simulations of the Rutgers experiments were generated, using a combination of the GE-645 computer at Bell Telephone Laboratories, Murray Hill, and the SDS-925 at Rutgers. The GE computer was used to do the time-consuming Monte Carlo calculations, and the final corrections were more efficiently performed with the aid of the display facility of the SDS-925. The various experimental dimensions that are necessary for the simulation were carefully measured. However, the exact thickness of the CD₂ targets was unknown.

The target thickness was determined by making several simulations with various thicknesses and comparing with the experimental data. This method appeared to be accurate to about 5%. In the case of the

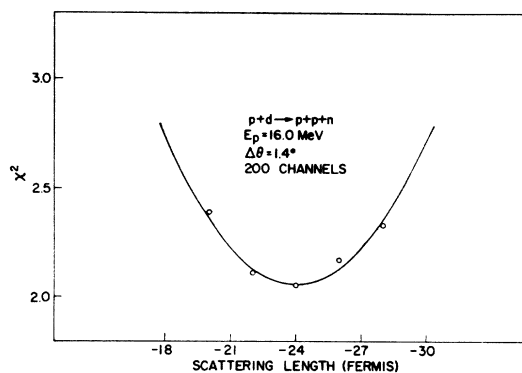


FIG. 15. Best χ^2 parabola for the high-resolution $p+d$ 16-MeV experiment.

CH₂ target, the thickness was accurately known by weighing, and the results of the simulation agreed with that value. The target-thickness correction program produced excellent fits to reactions having various charged reaction products over a wide energy range. Figure 8 shows simulations that have not had the effect of target thickness and detector energy resolution folded in. The broadening that these effects produce is seen by comparing Figs. 8(c) and 7(b).

The energy calibrations were adjusted by varying these parameters in the simulation and comparing with the experiment. In the worst case, this adjustment differed by only 100 keV from the nominal experimental value. A summary of the final experimental parameters of all the simulations appears in Table I.

D. Matrix Elements

The considerations of Sec. I D lead one to expect the reaction matrix element to be given by the product of two terms, one that represents the primary interaction (PI) and one that describes the final-state interactions (FSI).

The only production process that is observed to cause strong modulation of the cross section in the $p+d$ and $d+p$ reactions is the knockout process, or spectator effect, described in Sec. IV A. We therefore approximate the PI expression with the sum of two terms: A constant term that represents the production processes that have no strong final-state energy dependence, and a term describing the spectator effect,

$$M_{PI} = (1 - C_s) + C_s |\psi(P_n)|^2, \quad (7)$$

where C_s describes the strength of the spectator effect relative to the constant term, and $\psi(P_n)$ —the deuteron wave function in momentum space—describes the amplitude for the spectator effect, as explained in Sec. IV A. The constant C_s is left as an adjustable parameter, which must be fitted to the experiment. If the description of the production interaction given in Eq. (5) is not accurate, we might expect to find an apparent variation of C_s with the detection angles θ_3 and θ_1 . In any case, C_s would in general be expected to vary with the total center-of-mass energy.

The discussions of Sec. I D and IV A suggest that, assuming interference terms are small, the FSI term should be represented by the sum of the enhancement factors for each pair of particles, in each spin state. Thus, we may write

$$M_{FSI} = C_{34}^s E_{34}^s + C_{35}^s E_{35}^s + C_{45}^s E_{45}^s + C_{35}^t E_{35}^t + C_{45}^t E_{45}^t,$$

where the E_{ij}^k terms are the enhancement factors of Eqs. (2) and (3) (see Sec. I C).

Each term of this expression can be represented by one of the diagrams of Fig. 1. The five parameters C_{ij}^k describe the probability that the primary interaction leaves particles i and j in a relative s state with spin k , and the E_{ij}^k terms describe the resulting final-state

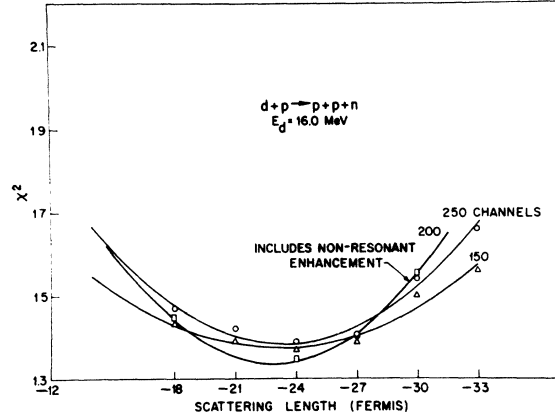


FIG. 16. χ^2 fits to the scattering length for the 16-MeV $d+p$ data. Since the sensitivity to the scattering length is greatly decreased for this run, an attempt was made to determine the effect of using a more complete theory for the background terms than is ordinarily necessary to get the peak shape. The improvement in the curvature when nonresonant terms are included is only very slight, as is evident by comparing the curve labeled "includes nonresonant enhancements" to the other two, which include only singlet and triplet enhancements from particles 4 and 5.

enhancement as a function of relative energy. In the high-resolution experiments, where the angles were selected to allow particles 4 and 5 to have a low relative energy, E_{45}^s is the strongest and most rapidly varying term.

The other enhancement terms are slowly varying and make up the background. The strength of this background can be measured in regions on either side of the peak, which we refer to as the "wings." The enhancements E_{pn}^s (p - n singlet), E_{pn}^t (p - n triplet), and E_{pp}^s (p - p singlet) are shown in Fig. 6.

The p - p enhancement E_{pp}^s goes to zero at low relative energy because of the Coulomb barrier. Since there is not enough structure in the cross section to determine all the C_{ij}^k parameters uniquely from these experiments, it is desirable to reduce the number of such free parameters. If we assume that the primary interaction produces virtual deuterons isotropically in the center-of-mass system, it follows that

$$C_{35}^t = C_{45}^t,$$

$$C_{35}^s = C_{45}^s.$$

At symmetric angles, such as in the 21.1-MeV $d+p$ experiment, this relation clearly holds independently of the assumption of isotropy. We therefore write

$$M_{FSI} = E_{35}^s + E_{45}^s + C_{pp} E_{34}^s + T/S (E_{35}^t + E_{45}^t), \quad (8)$$

where we have set

$$C_{35}^s = C_{45}^s,$$

$$C_{35}^t/C_{35}^s = C_{45}^t/C_{45}^s = T/S,$$

$$C_{34}^s = C_{pp},$$

and C_{35}^s and C_{45}^s have been normalized to unity. The

FSI's are thus described by just two adjustable parameters, the triplet-to-singlet ratio T/S and the p - p interaction strength C_{pp} .

The final form of the cross section will be

$$d^4\sigma/dT_3dT_4d\Omega_3d\Omega_4 = N \times M_{PI} \times M_{FSI} \times \rho,$$

where N is the over-all normalization, and the expression for phase space ρ is given in Sec. I E. There are four adjustable parameters in this expression: N , C_s , C_{pp} , and T/S . In addition, the singlet p - n scattering length will be treated as a free parameter in order to determine how accurately this parameter can be extracted from the data.

E. Comparison of Experiment to Theory

Figures 4, 7, 9, and 10 show full simulations of the various experiments. The experimental parameters used in the simulations are given in Table I, and the values of C_{pp} , T/S , and C_s , which produced best fits, are given in Table II. For these simulations, accepted values of scattering lengths and effective ranges were used.⁶⁷ These are given below in fermis:

$$\begin{aligned} a_s &= -23.68, & r_s &= 2.5, \\ a_t &= 5.40, & r_t &= 1.7, \\ a_{pp} &= -7.8, & r_{pp} &= 2.75. \end{aligned}$$

The relative contributions of some of the various enhancements in the FSI term are illustrated in Figs. 5 and 11. Figure 5, the $d+p$ 21.1-MeV enhancements, was discussed in Sec. IV A. Figure 10 is discussed in Sec. IV G. The simulations of Fig. 7 were projected onto the T_4 axis; these projections are shown in Figs. 12 and 13, along with the projected experimental data. The solid curves show the effect of varying the singlet p - n scattering length in the simulations. Figure 8 shows the effect of varying the scattering length in a two-dimensional simulation. Since projection causes the loss of much hard-won experimental information, the projection method is not the most satisfactory way to compare theory to experiment. Therefore, a program was written that measures the mean-square deviation of theory and experiment in any region of the two-dimensional energy array indicated to the computer by light pen.

Since the over-all normalization of the theory is arbitrary, we first normalize the theory to the data at a region (usually the top of the peak) indicated by light pen. This is done using a computer program that minimizes the variance of the selected channels. Once the normalization is completed, a region of interest in the spectrum is indicated by removing these channels from the display with the light pen. The computer then evaluates the expression

$$\chi^2 = N^{-1} \sum_i^N (X_i^{\text{sim}} - X_i^{\text{expt}})^2 / X_i^{\text{expt}},$$

⁶⁷ H. P. Noyes, Phys. Rev. **130**, 2205 (1963).

where X_i^{sim} and X_i^{expt} are the number of counts in the i th simulated and experimental channel, respectively, and N is the number of indicated channels. This expression is the normalized χ^2 deviation of the N channels indicated by the light pen.

In order to measure the sensitivity with which the experiment determines some parameters, e.g., the singlet p - n scattering length a_{pn}^s , we determine the variation of χ^2 with that parameter $\chi^2(a_{pn}^s)$. The minimum of this function determines the best value of a_{pn}^s . Providing that N is large, the χ_{min}^2 of a normalized χ^2 distribution are Gaussian-distributed, with an expectation value equal to 1, and with variance $(2/N)^{1/2}$. In addition, the error in any parameter, such as a_{pn}^s , can be determined by varying that parameter until χ^2 increases by $1/N$ above χ_{min}^2 while holding the other parameters fixed at their optimum values.⁶⁸

F. Extraction of Singlet p - n Scattering Length

Simulations of the three 16-MeV runs were performed with singlet p - n scattering lengths a_{pn}^s ranging from -18 to -33 F. For each simulation, the best value of T/S was determined, and the other parameters were held fixed at their previously determined optimum values. T/S must be varied, since changing a_{pn}^s changes the normalization of the singlet enhancements while the triplet enhancements are held fixed. This adjustment is made by varying the strength of the simulated "wings" to match those of the data. The function χ^2 is then computed for each value of a_{pn}^s , and the results are fitted to a parabola, using a least-squares fitting routine.⁶⁹

Figure 14 shows the resulting parabolas for the $p+d$, $\Delta\theta=2.0^\circ$ experiment at 16 MeV. In order to determine any possible systematic errors, the function $\chi^2(a_{pn}^s)$ was determined, using successively larger regions of the singlet p - n FSI peak. The four parabolas are labeled according to the number of channels included in the measured region: 150 channels include just the upper quarter of the peak; 300 channels include about two-thirds of the peak (measured from top to base). Since the width of the peak is the feature most sensitive to the scattering length, we would ideally expect to get the steepest parabola from the region that contains the greatest part of the peak, i.e., the 300-channel curve. This is seen to be the case in Fig. 14; however, the value of χ^2 at the minimum is larger when more channels are used, indicating that the theory departs from the data slightly in shape. The statistical uncertainty of these curves varies from 0.2 to 0.5 F, and the minima are found to range from 23.5 to 24.1 F.

In order to assign an uncertainty to the value of a_{pn}^s as obtained from these curves, many factors have to be considered. In addition to the statistical uncertainties of 0.2–0.5 F and the fact that the minima

⁶⁸ R. J. Plano (unpublished).

⁶⁹ Subroutine QUADFIT, written by D. H. Wilkinson, F. R. S., Professor of Experimental Physics, University of Oxford.

depend on the range of data considered, there are errors introduced by the uncertainty in the exact shape of the χ^2 curve, which was assumed to be parabolic, and by the difficulty in optimizing all of the many simulation parameters (Table I). We believe that these effects combine to produce an over-all uncertainty of ± 0.5 F, and the value of the scattering length obtained in this way is -23.8 ± 0.5 F.

In order to determine whether broadening effects were limiting the accuracy with which we could extract a_{pn}^s , a second run was taken with smaller solid angles: $\Delta\theta = 1.4^\circ$. These data are shown in Fig. 7(d). The FSI peak is narrower and contains about twice as many counts at the maximum as Fig. 7(b). This improvement in resolution resulted in a χ^2 curve (Fig. 15) that does not have as low a minimum as Fig. 14. This is explained by a small departure in shape of the simulation from the experiment, which may indicate the limit to which the simulation technique in its present form can account for broadening effects. The minimum of the parabola shown in Fig. 15 is at 23.9 F, but, as before, this value was found to vary by ± 0.5 F, depending on many factors, such as the way in which theory and experiment were normalized, exactly which channels were selected for the χ^2 comparison, etc. As a final check, χ^2 parabolas of the projected spectra of Fig. 12 were made. These were steeper than in Fig. 15, but their minima agreed with the results of the full two-dimensional comparisons and showed the same variations.

Figure 16 shows $\chi^2(a_{pn}^s)$ parabolas obtained from the $d+p$ 16-MeV experiment. The steepest parabola was obtained by using the complete FSI enhancement factor [Eq. (8)], which includes the interactions of all pairs of particles. In order to test the sensitivity of the fit to the details of the theory, the other two parabolas show the result one obtains if we set

$$C_{35}^s = C_{35}^t = C_{31}^s = C_s = 0,$$

so that

$$M_{\text{FSI}} = E_{45}^s + T/SE_{45}^t.$$

In this enhancement factor, only the contribution from the two "resonating" particles (4 and 5) is included, and the effect of leaving out the nonresonant processes is compensated for by using a larger value for T/S . These parabolas show a slight decrease in sensitivity to a_{pn}^s and the same minimum within the fitting error. In the $p+d$ 16-MeV experiments, there is essentially no difference between parabolas that use the full FSI term or those that use the abbreviated one.

The $d+p$ parabolas have considerably less sensitivity to the scattering length than the $p+d$ ones. This decrease in the sensitivity to a_{pn}^s at lower c.m. energies is explained by the relatively stronger background present under these conditions. Even a careful adjustment of the shape of the background, such as is obtained using the complete FSI term, does not compensate for the lack of sharpness of the peak. The statistical error is 1.5 F for the shallow curves and 1.0 F for the steeper one. How-

ever, a consideration of the effects discussed for the higher-energy data increases this uncertainty to 2.0 F. We thus extract from this run a value of a_{pn}^s of -23.5 ± 2.0 F (see Table II).

In the 10-MeV $d+p$ data (Fig. 10), the background from nonresonant processes is so large that it was not possible to extract a very meaningful value of a_{pn}^s . The value of this experiment lies in elucidating the behavior of the parameters that describe the background, i.e., T/S , C_s , and C_{pp} .

G. Discussion of Other Parameters—Effective Range

As shown in Eq. (2) the FSI enhancement factor depends on the effective range r_0 . Therefore, the experimental peak width does not determine uniquely the scattering length if r_0 is unknown. The error we would make by neglecting r_0 entirely (setting $r_0=0$) is measured by the expression

$$\frac{1}{2}r_0^s k^2 / (1/a_{pn}^s - \frac{1}{2}r_0^s k^2).$$

If we confine our attention to the region of the singlet FSI peak above its half-maximum point, i.e., $k < k_{1/2}$, then this error will be about 5% in the derived value of a_{pn}^s , since $r_0^s/a_{pn}^s \leq 0.1$ and $1/a_{pn}^s \leq k_{1/2}$. However, if r_0^s were substantially larger than $0.1a^s$, then the effect of the $\frac{1}{2}r_0^s k^2$ term becomes more significant. As a check of this reasoning, full simulations were performed, using $r_0=3.6$ F rather than its accepted value of 2.4 F. It was then found that best fits were obtained with scattering lengths of about -30 instead of -24 F. This assumes considerable importance if the method is to be used to extract accurate scattering lengths for particle interactions where the effective range is poorly known, e.g., the $n-n$ interaction.

Triplet-to-Singlet Ratio

It was found that the value for the triplet-to-singlet ratio T/S seems to increase from 2 to 5 as we go from 8.44 meV to 1.1 MeV in center-of-mass energy (see Table II). If we assume that the diagrams of the single-interaction model (Fig. 1) are formed with equal probability for each spin state, then we would expect T/S to be 3 or greater, allowing a spin degeneracy of 3 for each of the triplet graphs. A value of 3 would be appropriate if the doublet scattering dominates, and a value of 6 would be expected for the case that the doublet and quartet diagrams have equal probability, etc. Brückmann *et al.*²² studied the dependence of T/S on θ_5 at fixed energy (52-MeV deuterons). They found a large variation, which had a minimum of $T/S=0$ at $\theta_{5 \text{ c.m.}} = 60^\circ$. These large variations in T/S are manifestations of primary reaction effects, which are poorly understood at the present time.

Nonresonant Terms

By referring to Fig. 6, we see that the contributions from the various enhancements increase several times as we go from >6 - to 1-MeV relative energy. Since the

relative energy between any two particles can be, at most, the total c.m. energy, this means that the relative contribution from "nonresonant" interactions will increase as the c.m. energy decreases. We therefore expect the background to increase substantially as we go from high center-of-mass energy (8.44 MeV in the 16-MeV $p+d$ runs) to low center-of-mass energy (1.11 MeV in the 10-MeV $d+p$ run).

Figures 11(a)–(d) show the terms E_{35}^s , T/SE_{35}^t , E_{15}^s , and T/SE_{45}^t in the proportion that they contribute to the full $d+p$ 10-MeV simulation of Fig. 10. In this experiment, the angles were selected to allow a low relative energy between particles 3 and 5, and the resulting broad singlet FSI peak is shown in Fig. 11(c). Particles 4 and 5 contribute as the nonresonant enhancements of Figs. 11(a) and 11(b). The full simulation with $T/S=5$, $C_{pp}=5$, and $C_s=0.5$ is a very good fit to the experimental data, except for a small deficiency in the wing at high T_3 energy, in the region where the (4, 5) enhancement is increasing. The fact that our FSI matrix element can produce excellent fits even at such low center-of-mass energies lends additional confidence to its use.

Since the various background terms do not show much structure, the parameters C_{pp} , C_s , and T/S cannot be determined independently with accuracy. Many simulations were made with various combinations of parameters, and it was possible to estimate what the errors in these parameters might be if they were allowed to vary freely. The errors are tabulated in Table II. These parameters could be more accurately determined if we expanded the spectrum to include the entire kinematic line, as in the 21.1-MeV $d+p$ experiment. However, for the purposes of extracting the $p-n$ scattering length, we do not need to know them accurately.

H. Interference Effects

In order to determine whether the interference effects discussed in Sec. I D might be important in our experiments, the FSI matrix element of Eq. (8) was modified according to Eq. (4), so that

$$M_{\text{FSI}} = E_{15}^s(1 + C_{\text{int}}k_{45}) + E_{35}^s + C_{pp}E_{34}^s + T/S(E_{35}^t + E_{45}^t).$$

Full simulations of the 16-MeV $p+d$ data with $\Delta\theta=2^\circ$ were made using this expression. If we assume constructive interference and use the measured quantities of C_{pp} and T/S from Table II,

$$(C_{\text{int}})_{\text{max}} = 2[C_{pp}^{1/2} + (T/S)^{1/2}]/k_{pp} = 0.025.$$

Such a value of C_{int} produced a shift in a_{pn}^s of 6 F. Due to phase cancellation, C_{int} and the shift in a_{pn}^s are likely to be much smaller, and this indeed seems to be the case, since the extracted value of a_{pn}^s is in agreement with its known value to within 0.5 F.

$(C_{\text{int}})_{\text{max}}$ increases at lower center-of-mass energies, and hence the two $d+p$ runs should be more sensitive

to interference effects. Unfortunately, the sensitivity of these experiments to a_{pn}^s is also decreasing, and consequently, we cannot say for sure whether there is interference or not at lower energies.

V. CONCLUSIONS

Coincidence studies of three-body final states have the advantage of maximally isolating the FSI of interest from background processes. As can be seen from Fig. 7(c), the nonresonant background under the FSI levels of interest can be made both very small and quite flat. Consequently, it is not necessary to describe this background in detail in order to parametrize accurately the FSI. For such experiments, it is found that a simple theory containing three adjustable parameters can adequately account for all the structure of the experimental data. This theory treats the singlet and triplet pair interactions of all the final-state particles by means of additive enhancements and accounts for spectator effects. With this description, it is possible to extract accurately the singlet $p-n$ scattering length from data at c.m. energies greater than a few MeV. The success of these experiments in predicting the known scattering length indicates that interference effects that could distort the shape of the FSI cross section are not significant, under the conditions of the investigation. We would expect that these conclusions should correspondingly hold true for the $n+d$ reaction; this would make possible the extraction of an accurate $n-n$ scattering length, using similar techniques. However, in the $n-n$ case, some ambiguity would still remain, in that the value of the scattering length will depend to some extent on the assumed magnitude of the effective range, especially if it were larger than 1.5 F.

The analysis presented here indicates that even greater accuracy could be achieved in extracting a_{pn}^s if higher center-of-mass energies and smaller solid angles were used. In addition, it should be interesting to perform higher-resolution experiments at low c.m. energy in order to determine the limit of applicability of FSI theory.

ACKNOWLEDGMENTS

The authors are indebted to Dr. J. P. F. Sellschop, Dr. D. J. Bredin, P. Assimakopoulos, and B. Marsh for their contributions to the experimental work, and to Dr. Č. Zupančič, Dr. D. H. Wilkinson, and Dr. J. G. Taylor for discussions and suggestions on the interpretation of the results. Credit is due R. C. Petersen and the members of the tandem staff who were responsible for the excellent performance of the accelerator throughout this research.

APPENDIX

A. Three-Body Simulation Program

The basic philosophy of the simulation program is discussed in Sec. II B. A partial listing of the FORTRAN statements is included in Ref. 23.

In order to optimize the use of the computer memory, the program is divided into several sections called links, which may operate in any desired sequence. Each link performs operations on a 64×64-channel data array.

Without disturbing this data array, the links are successively loaded into memory from magnetic tape in an order specified by a link list, which is provided as input data. Normally, the first link will be the main simulation program, which performs the Monte Carlo integration over the solid angles. Since this program is time consuming, two versions are available, one which runs on the SDS-925 at Rutgers, and a computation center version which runs on a GE-645 at Bell Laboratories and computes for several theoretical parameters simultaneously. The result of the GE-645 calculation is punched on cards that can be read into the SDS-925 computer, where the other links are most efficiently executed.

The main simulation program reads the necessary input parameters such as masses, the dimensions of the detector and beam collimators, detector angles, beam energy, energy calibration, and the desired number of Monte Carlo events.

For each of the Monte Carlo events, random points are selected within the geometric limits specified by the beam spot, detector collimators, and a multiple-scattering angle. The angles of particles 3 and 4 are calculated from these points.

A kinematic locus is then calculated channel by channel, forming a T_3 - T_4 spectrum. These solutions are calculated using two DO loops: One steps along the T_3 axis channel by channel; the other interchanges the role of the T_3 and T_4 axes and steps through the channels again. The T_4 kinematic solutions corresponding to the T_3 energies are then calculated. Phase space is calculated as described in Sec. I E and is multiplied by the matrix elements described in Sec. IV D. The kinematic solutions and corresponding cross sections for each kinematic loop are stored. At the completion of each loop, the SDS-925 program writes the results on magnetic tape for later analysis; the GE-645 program adds it directly into the 64×64 channel data array. The SDS-925-generated results are added into the 64×64-channel data array by a new link, which has available sufficient memory space to store 4098 channels.

B. Target-Thickness Correction

The result of the main simulation program may now be corrected for the energy loss of the beam and detected particles by executing the target-correction link. The energy loss in CH_2 and CD_2 targets is computed using

the expression

$$E_{\text{loss}} = (0.1428mz^2/E)(X/A)\{8.0 \ln(E/M) + 30.9\},$$

where X and A are the target thickness in mg/cm^2 and its molecular weight. m , z , and E are the mass in amu, charge number, and kinetic energy in MeV of the projectile.

In order to obtain an integration over the target thickness, the target is divided into N layers. The resulting energy corrections to the T_3 - T_4 data array are computed for each layer and the results averaged. The energy loss of the projectile is accounted for by using the approximation that this energy loss is shared among the three final particles in proportion to their energies.

C. Energy Resolution of Detectors

The 64×64-channel data array is corrected for the effect of the detector resolution by folding in a Gaussian function whose width is given by an experimentally measured resolution function. The correction to the data array is given by the following convolution integral:

$$\rho(T_3, T_4) = \int_0^\infty \int_0^\infty \exp\left(-\frac{(T_3 - T_3')^2}{0.73\sigma_3}\right) \exp\left(-\frac{(T_4 - T_4')^2}{0.73\sigma_4}\right) \times \rho(T_3', T_4') dT_3' dT_4',$$

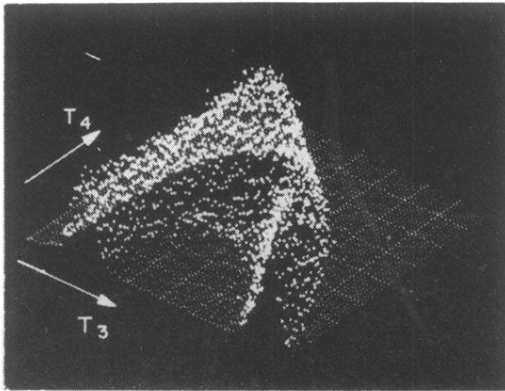
where σ_3 and σ_4 are the full widths at half-maximum of the detector resolution functions. This integral is calculated numerically by the energy-resolution link. The exponential functions are approximated by step functions, where each step is the width of a T_3 or T_4 channel. The contribution of each step is calculated, and, after averaging, the corrected array $\rho(T_3, T_4)$ results. For cases in which the resolution function was not Gaussian, an option is available that folds in the actual experimental detector resolution function, as measured with a pulser.

D. Energy-Calibration Correction

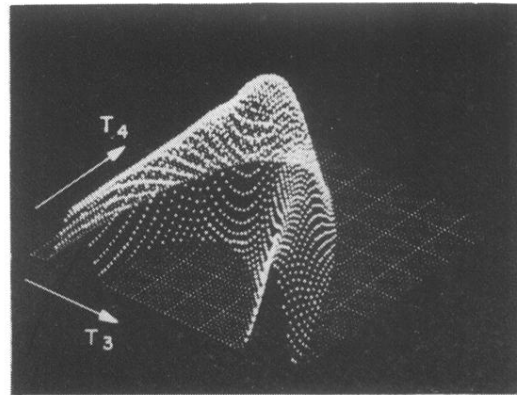
The exact channel location of the simulated T_3 - T_4 spectrum depends on the energy calibration of the T_3 and T_4 axes. If it is desired to change this energy calibration and thereby shift the location and scale of the simulation, the energy-calibration link may be used. This transformation is simply performed by using DO loops, which first calculate and adjust the T_3 energies and then the T_4 energies. The effect of the transformation may be judged using the display link, which displays theory and experiment alternately and includes an option for subtracting theory from experiment.

$d+p \rightarrow p+p+n$

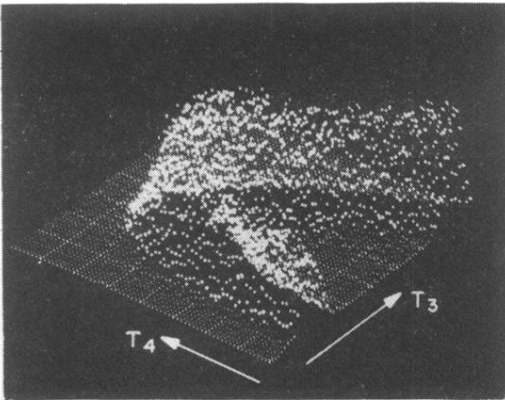
$E_d = 10.0 \text{ MeV}$



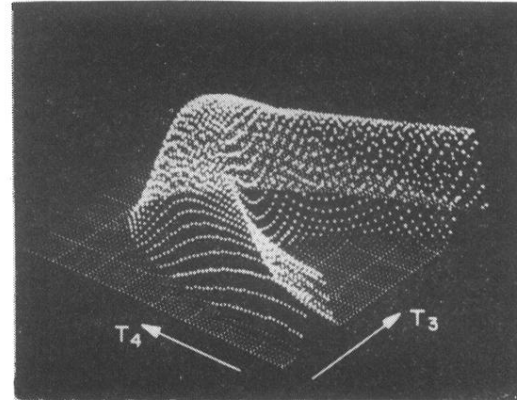
(a) EXPERIMENT



(b) THEORY

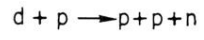


(c) EXPERIMENT

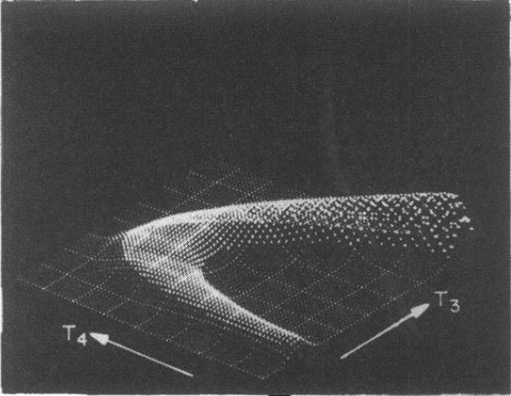


(d) THEORY

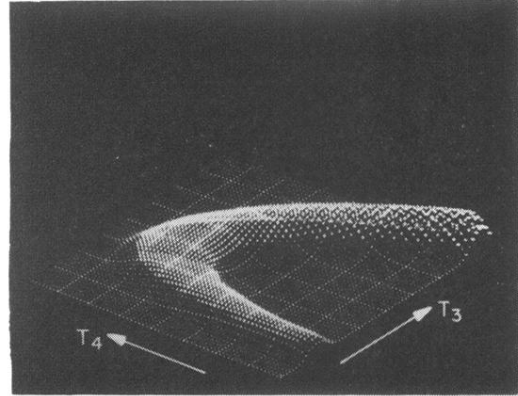
FIG. 10. Comparison of the $d+p$ 10-MeV data with theory.



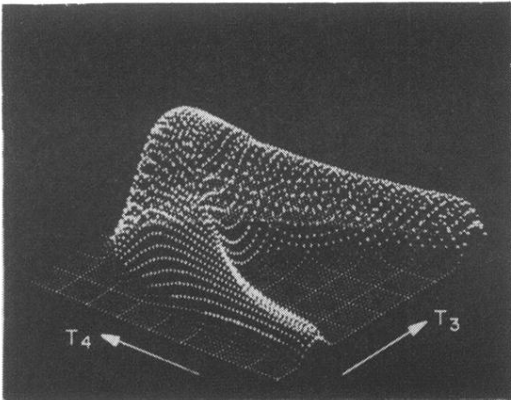
$$E_d = 10.0 \text{ MeV}$$



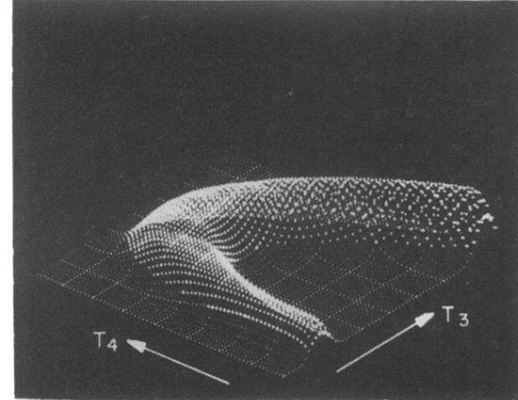
(a) NON RESONANT SINGLET
ENHANCEMENT



(b) NON RESONANT TRIPLET
ENHANCEMENT

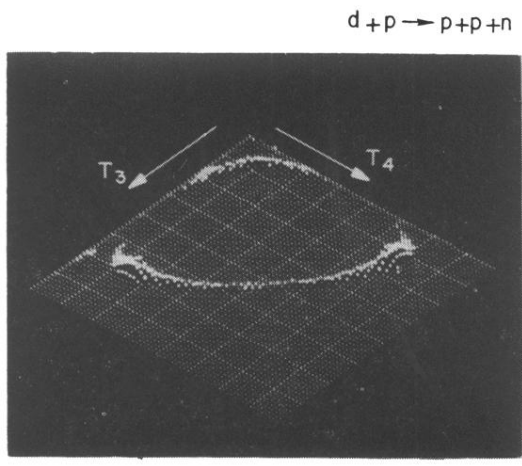


(c) RESONANT SINGLET
ENHANCEMENT

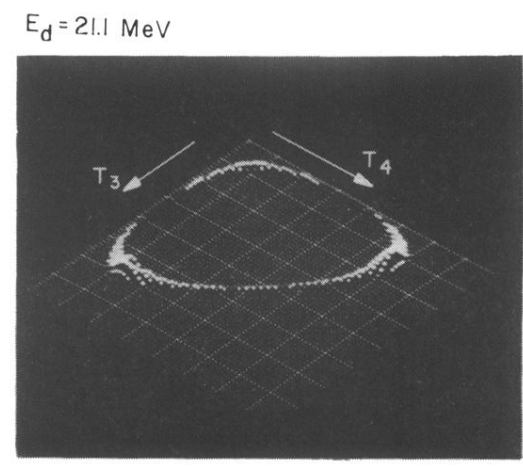


(d) RESONANT TRIPLET
ENHANCEMENT

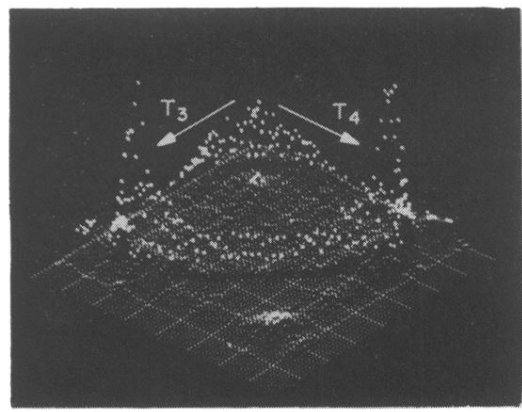
FIG. 11. (a) and (b). Singlet and triplet enhancement factors for the "nonresonant" particles 4 and 5. (c) and (d). The same enhancements for the "resonant" particles 3 and 5, which are formed with low relative energy.



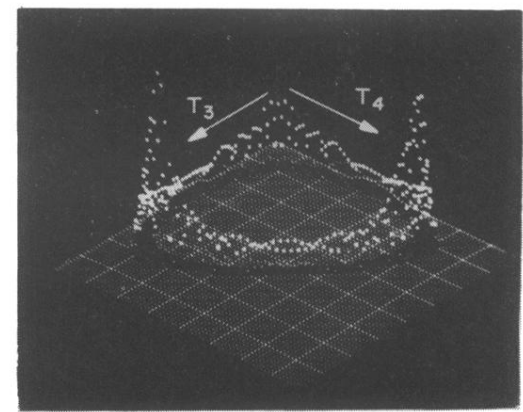
(a) EXPERIMENT



(b) THEORY



(c) EXPERIMENT



(d) THEORY

FIG. 4. Comparison of $d+p$ 21.1-MeV data with a complete simulation. *a* and *b* are at low count gain, and *c* and *d* at a higher count gain (see text).

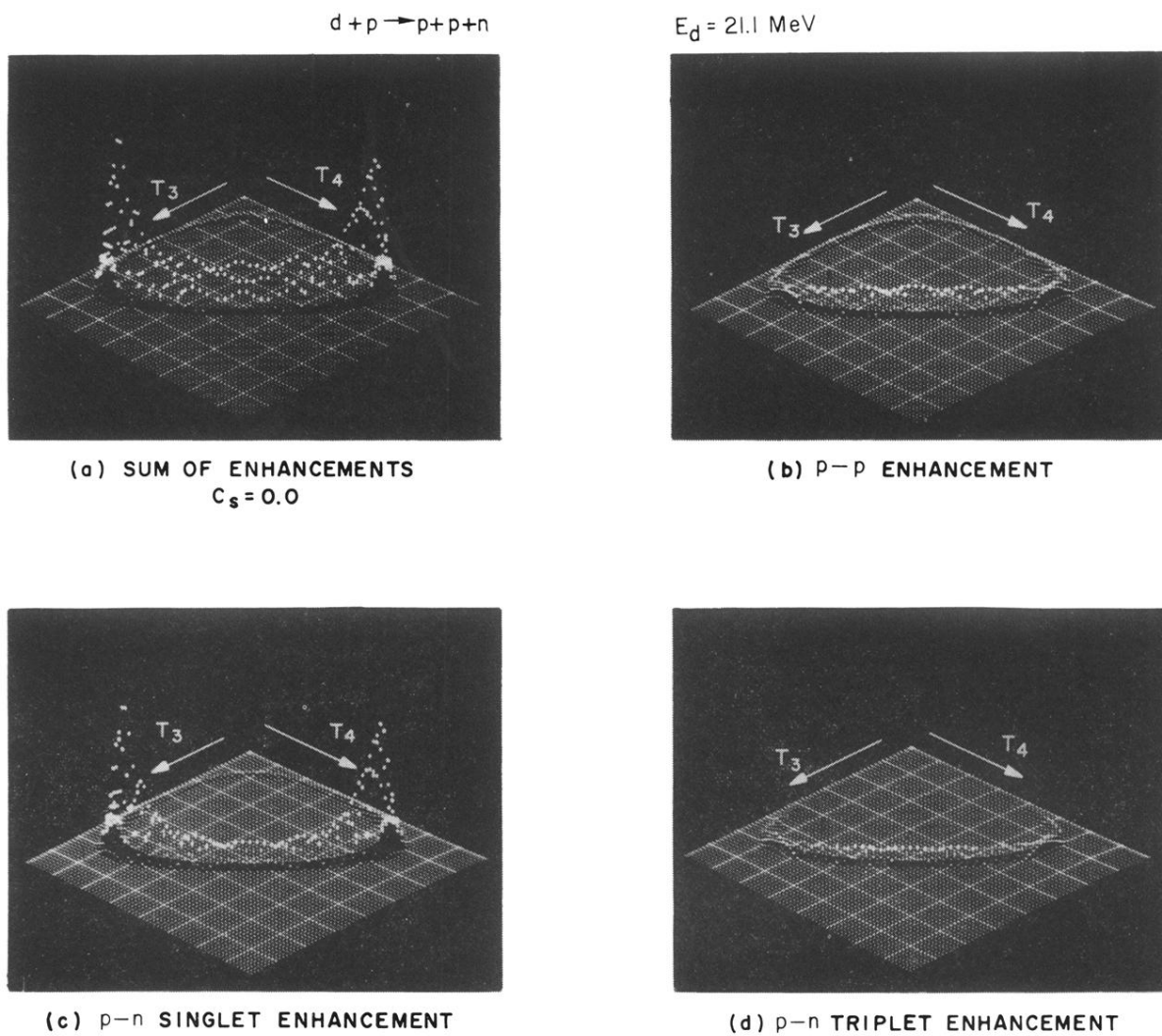
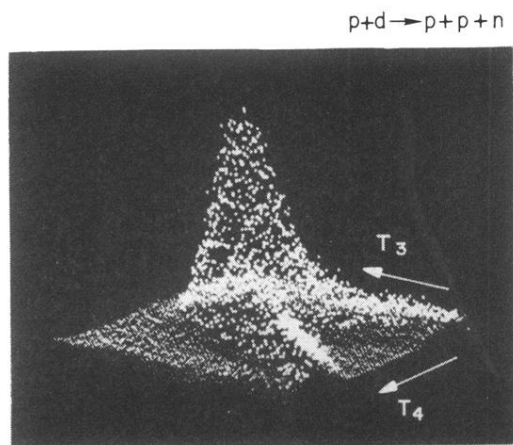
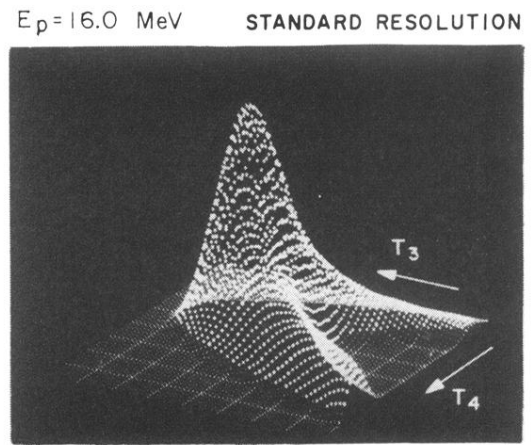


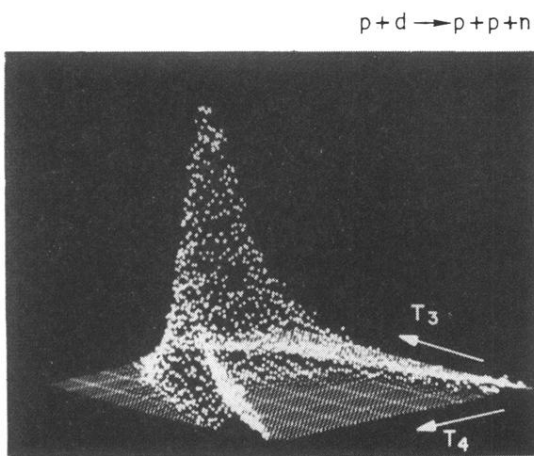
FIG. 5. Simulations using various enhancement factors for the $d+p$ reaction at 21.1 MeV in (b), (c), and (d); their sum in (a).



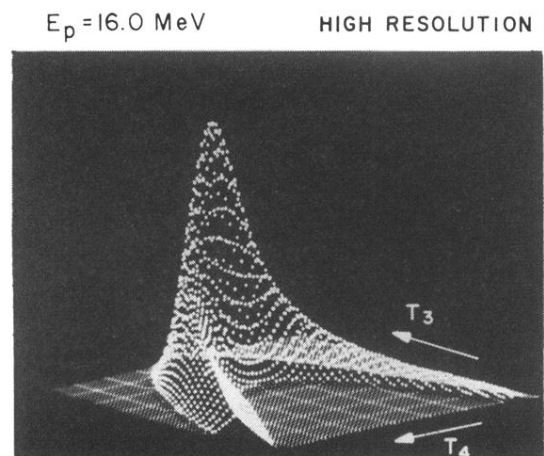
(a) EXPERIMENT



(b) THEORY



(c) EXPERIMENT



(d) THEORY

FIG. 7. Comparison of the $p+d$ 16-MeV data with theory. In (a) and (b) angular widths of the detectors were 2° . In (c) and (d) these widths were set to 1.4° in order to increase the resolution of the experiment. The resulting FSI peak is much narrower than its counterpart in (a) and (b).

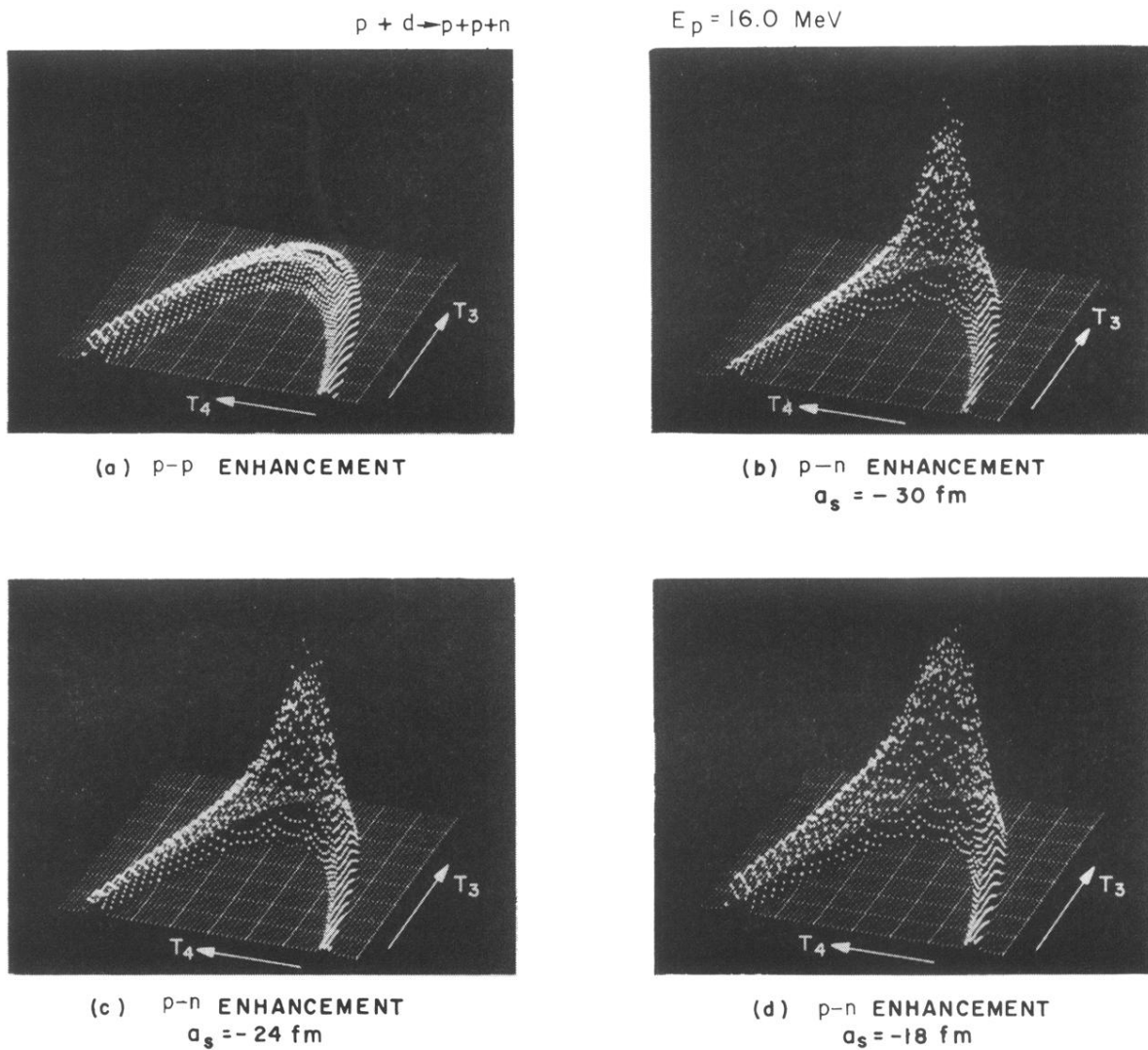
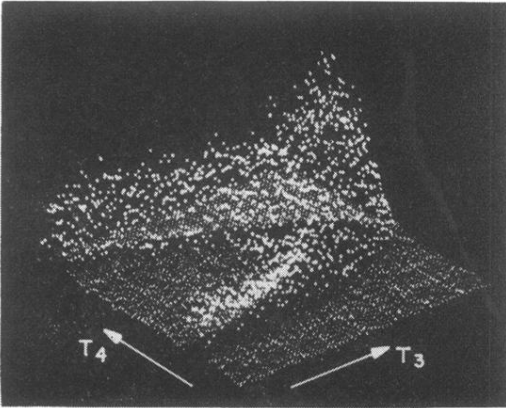


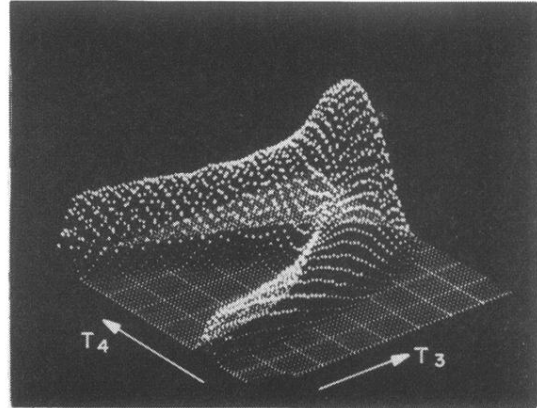
FIG. 8. Raw Monte Carlo simulations of the 16-MeV $p+d$ experiment without the smearing due to target thickness and detector energy resolution being folded in. The effect of varying the singlet p - n scattering length for particles 4 and 5 is illustrated in (b), (c), and (d).

$d+p \rightarrow p+p+n$

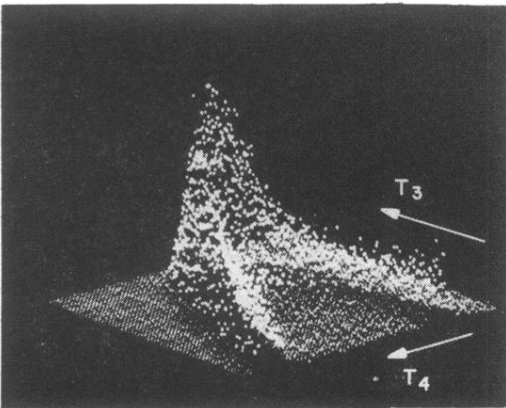
$E_d = 16.0 \text{ MeV}$



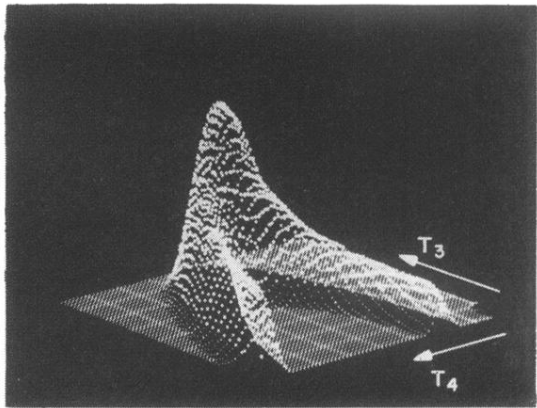
(a) EXPERIMENT



(b) THEORY



(c) EXPERIMENT



(d) THEORY

FIG. 9. Comparison of the $d+p$ 16-MeV data with theory from two perspectives.